Development of an analytical model for a special design asynchronous motor

Wan Li

Master of Science Thesis

TU Delft Delft University of Technology

Challenge the future

Development of an analytical model for a special design asynchronous motor

by

Wan Li

to obtain the degree of Master of Science
at the Delft University of Technology,
to be defended publicly on 23, August, 2019.

Student number: 4741293
Project duration: December 1, 2018 – August 23, 2019
Thesis committee:

Prof.dr. Pavol Bauer,	TU Delft,	supervisor
Dr.ir. Jianning Dong,	TU Delft,	supervisor
Prof.dr. Arno Smets,	TU Delft	
Dr.ir. Peter Bax,	Philips	

TU Delft

Preface

The purpose of this research is to understand the performance of the special design asynchronous motor. The aim is achieved by the simulation with the finite element method in ANSYS and the analytical modeling in MathCAD. The research ends with a well-performing prototype and a developed analytical model. In this thesis, the research problem and the process are described. The corresponding solving methods and tests are presented.

During the 9 month research process, I would like to give my sincere thanks to Peter Bax. With your strong support and patient guidance, I experienced the pleasure of getting progress step by step within this topic and I truly love what I have been doing for this research. This research would be a valuable experience during my whole life. Then I want to give my appreciation to my supervisors. Thank you for your understanding and support during the whole process.

At last, my love and deepest gratitude go to my parents. Thanks for your respect, supporting and unconditional love.

Thanks all of those who encourage me and share with me my worries, frustrations and happiness.

Wan Li
Drachten, August 2019

Contents

1

Introduction

Electrical motors have been used in various fields for hundreds of years. The asynchronous motor is always an interesting topic. Because of the advantages of the simple structure, robustness, low maintenance cost and the long lifetime [1], the asynchronous motor has been widely used in lots of applications, for example, in pumps, blowers, compressors [2], hybrid electric vehicle [3], high-speed transit or subways as a traction motor [4].

1.1. Background

The most well-known design of the asynchronous motor is the squirrel cage rotor [5, 6] shown in Figure 1.1a. It consists of the conductive bars, the iron layer, and the end ring. Due to the conductive bars on the rotor looks like a squirrel-cage, the motor is named squirrel-cage asynchronous motor. To declare the functionality of the rotor parts, the working principle is explained in general here. The AC current in the stator winding generates the rotating magnetic fields, which induces the electromotive force (emf) at the rotor conductive bar. As a result, the eddy current flows in the rotor conductive bars. Because the conductor placed in a magnetic filed experiences the force, the rotor is able to rotate. In order to close the current path, two end rings are placed at the top and the bottom of the rotor.

It can be seen that, to make a fully functional rotor, the iron layer is needed to provide a complete magnetic flux path. The conductive layer and the end rings are provided to close the eddy current path. However, with the necessary parts, there are other possibilities for the rotor structure. As shown in Figure 1.1b, the copper layer functions as the conductive bar in Figure 1.1a. The iron layer inside the copper layer provides the path for the magnetic flux generated by the stator winding.

(a) Squirrel cage rotor (b) New design rotor

Figure 1.1: Classical and new design motors.

1.2. Research methodology

The methodology used in this research is described in this section. In the previous studies, some approaches are raised to characterize the asynchronous motor. In [2], the stator resistance measurement is performed to obtain the winding resistance while the motor is standstill. The magnetizing reactance and the resistance can be tested in free acceleration process and the parameters for the motor equivalent circuit can also be obtained by blocked-rotor test. These classical measurement methods are common to be learnt in textbooks [7]. The classical measurements are used in this research to determine several physical quantities, such as the winding resistance and the self-inductance.

Except the measurements, the simulation and modeling are two effective tools to understand and improve the motor performance in this research. The finite element method (FEM) is a vital computational method in simulations [8–10]. FEM can predict how the structure behaves under different environment and situations, such as different load, heat or vibrations, by solving the partial differential equations. FEM divides the whole geometry model into lots of small pieces which are called elements. Then FEM provides the numerical solution on each element and all the solutions are integrated into equations to model the whole system. Users can evaluate the structure performance before real producing.

The typical workflow of FEM is pre-processing the parameter values, building the geometry (model), meshing the geometry into elements, applying the boundary conditions, computing, and post-processing the results. In this research, ANSYS is the simulation software where FEM is applied. Besides the ANSYS simulation, an analytical model provided by Dr.ir.P.J.Bax from Philips TEG, is studied and developed. This analytical model describes and evaluates the motor with mathematical equations in the software named MathCAD. Comparing the simulation results from ANSYS with the modeling results from analytical model is taken as one of the ways to validate the method effectiveness.

After the above simulation and modeling verification, a prototype is built for the real tests and validations. In conclusion, the methodology used in this

research can be listed as follows.

- The classical measurement methods to obtain the basic physical quantities.
- The FEM simulation in ANSYS to simulate the motor performance.
- Comparison between the analytical modeling results in MathCAD with the simulation results.
- Realize the methods into prototype to do tests and validations.

1.3. Objectives

The objectives of this research are raised based on the problems which need to be solved. The existing analytical model is not good enough to explain the measurement results and the influence of the higher space harmonics are not clear. Based on the problems, the objectives of this research are to understand the motor performance, to solve the occurred problem and to verify the effectiveness of the solving method. In general the objectives are listed as follows.

- Understand the motor performance and verify the reason that leads to the problem.
- Develop the analytical model and build a simulation model in ANSYS to give more realistic simulation results.
- Propose the method to solve the problem and reason the choice.
- Validate and test the prototype and compare the tests results with the modeling results.

1.4. Assumptions for the research

Figure 1.2 shows the BH curve used in the simulations in the research. The maximum magnetic field in the simulations is below 0.3 T, which is far more below the saturation, and the BH curve within this magnetic field range can be taken as a straight line with certain slope. That leads to the first assumption that the system can still be taken as a linear system in the simulation.

The three phase AC voltage is generated by an electronic device inverter. The output is not perfect sinusoidal waveform which may contain harmonics. But the influence from the electrical device is ignored due to this is not the focus of this research. In the future research, three phase source with perfect sinusoidal waveform can be generated with more precise equipment or techniques [12].

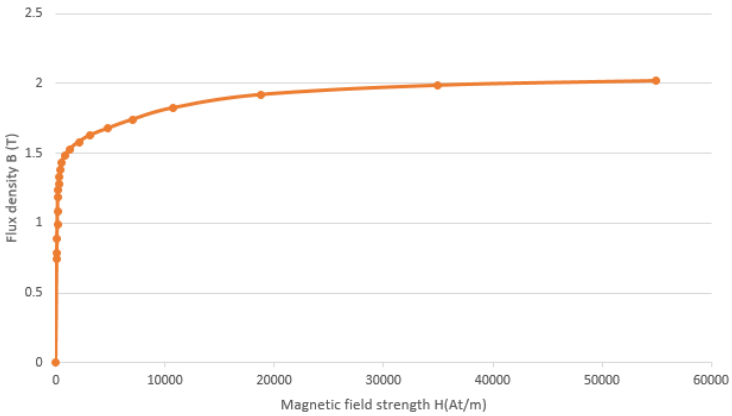

Figure 1.2: BH curve used in ANSYS simulations for all iron parts.

1.5. Basic performance parameters

To provide a general overview of the performance parameter of the 24 slots asynchronous motor in this research, Table 1.1 lists the basic parameters under no load operation for 65Hz driving frequency, which can also be found in the research results in Chapter 5 and Chapter 6.

Table 1.1: Basic performance parameter of the 24-slot asynchronous motor under no load operation for 65Hz driving frequency.

Stator slots	Motor Poles	Power (W)	Speed (rpm)
24	2	43.4	3202
Efficiency (%)	Start-up torque (N· m)	Peak torque (N· m)	
34.4	0.0148	0.0165	

1.6. Contributions

Due to this is the project between Philips and Delft University of Technology. It is necessary to declare the contributions from Philips and the author. Dr.ir.P.J.Bax from Philips TEG provides the important analytical model in Mathcad, the preliminary prototype of the new designed motor and the problem assumption as the fundamental knowledge for this research. Philips' workshop contributes to the producing of the motor prototype after the design. With the guidance of Dr.ir.P.J.Bax, the author derived the scheme to suppress certain harmonics for the 24-slot motor; build the simulation model in ANSYS and compare the results with analytical model to validate the method effectiveness. The author uses the stator provided by the workshop to make test windings and perform the prototype validation tests. In this thesis, the focus is put on the author's contributions while the analytical model provided by Dr.ir.P.J.Bax is described in general.

2

Problem description

Based on the new design rotor, a six slots asynchronous motor prototype is provided and some research about this motor has been done during the previous studies [11]. In this section, some tests for the six slots asynchronous motor are carried out to locate and describe the problem.

2.1. Loaded test

A preliminary prototype of this new design asynchronous motor with six stator slots is provided by Philips. To characterize this motor, a DC motor is coupled with the asynchronous motor as shown in Figure 2.1.

The torque speed characteristic curve (load curve) is a common way to observe the motor performance [13]. The test circuit to obtain the load curve is shown in Figure 2.2. An electronic inverter is connected to a DC source to generate the three phase AC voltage of which the phase difference is 120°. The three phase AC asynchronous motor is in Y connection. The Root-mean-square

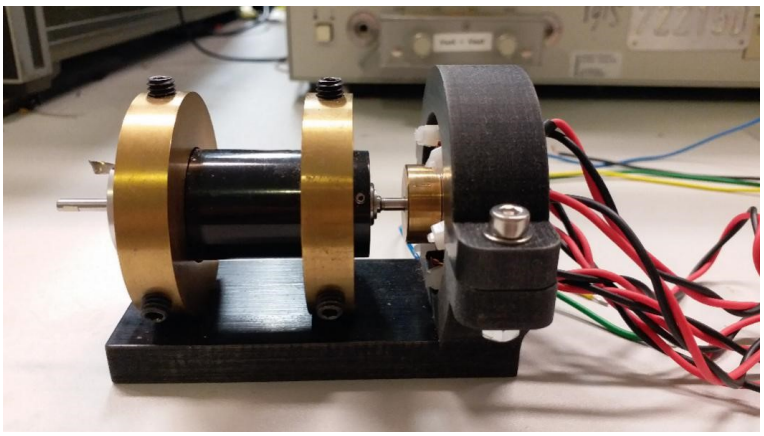

Figure 2.1: Preliminary prototype for six slots new designed motor coupled with DC motor.

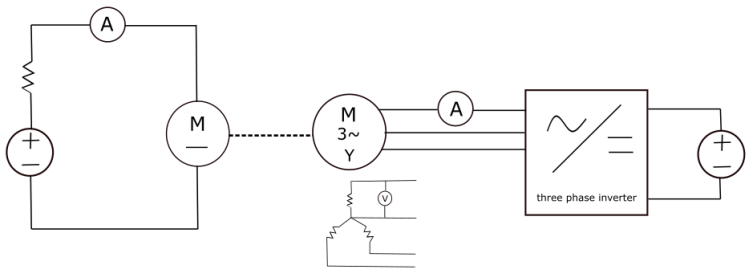

Figure 2.2: Preliminary prototype characterize circuit.

(RMS) value for phase current and voltage are measured by multi-meters. A DC motor is coupled with the asynchronous motor and a resistance with various values is added to provide multiple loads. A multi-meter is also connected in series to measure the load current. The DC motor can function as a load for asynchronous motor. It can also help or against the rotation of the asynchronous motor.

Equation (2.1) is used in plotting the load curve. T_{load} indicates the output load torque; k_{em} is the motor constant which can be obtained with the loaded tests; I_{load} is the load current; T_f represents the torque generated by the frictions at the motor shaft or other parts of the load. The friction torque can be expressed as $T_f = T_c + \omega/R_v$, where T_c is the coulomb friction torque; R_v is the viscous friction resistance and ω is the rotation speed. The values of T_c and R_v are obtained during the no-load test and the friction torque speed (T_c-ω) curve are provided by Dr.ir.P.J.Bax. With the T_c-ω curve, the voltage and rotational speed is measured while the asynchronous motor is loaded. The measurement data are shown in Table 2.1.

$$T_{load} = T_f - K_{em} * I_{load}. \tag{2.1}$$

Table 2.1: Loaded test data with electrical frequency 200HZ for six slots asynchronous motor.

$I_{load}(mA)$	78.8	59.2	37.5	14.5	3.1	1	0	-19.9	-28.9	-40.1
$U_{RMS}(v)$	3.99	3.99	3.99	3.99	3.99	3.99	3.93	3.93	3.93	3.93
$I_{RMS}(A)$	1.08	1.1	1.12	1.13	1.13	1.14	1.15	1.15	1.15	1.16
N (rpm)	2235	8851	8261	7103	6361	5627	5449	5414	4029	3191
$I_{load}(mA)$	-49.3	-60	-67.5	-114.9	-128.9	-134.8	-140.9	-152.8	-162	-169.5
$U_{RMS}(v)$	3.93	3.93	3.93	3.93	3.93	3.93	3.93	3.93	3.93	3.93
$I_{RMS}(A)$	1.16	1.17	1.17	1.17	1.17	1.17	1.18	1.19	1.2	1.22
N (rpm)	1310	164	0	0	545	1204	2133	3231	4258	5223

With the measurement data and Equation 2.1, the load curve of the six slots asynchronous motor can be plotted as Figure 2.3. For a well-performing asynchronous motor, the load curve is expected to be as what is shown in Figure 1 in [13], which is the typical torque-speed characteristic of an asynchronous machine. However, it can be seen from the figure that the load curve for the

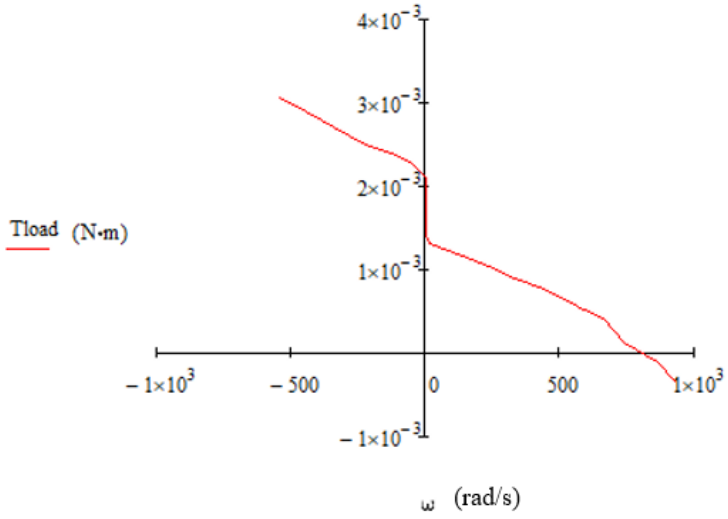

Figure 2.3: Torque speed characteristic curve of the six slots asynchronous motor.

six slots asynchronous motor does not perform even close to what is shown in Figure 1 in [13]. To find out the reason, simulation and modeling are used to help the analysis.

2.2. General description of the analytical model

Dr.ir.P.J.Bax from Philips TEG provides an analytical model built in the software named MathCAD as an important fundamental modeling study material [14]. This model is the basis for the further development in Chapter 6. To give a general explanation, the method of building this model is described in a flow chart as Figure 2.4.

- Define the description parameters, including the winding resistance, number of slots, winding turns, direction and distribution, etc.
- Use the mathematical equations to express the magnetic field distribution.
- Obtain the Fourier coefficients of the magnetic field density distribution waveform.
- Express the travelling magnetic field into sinusoidal functions with the Fourier coefficients.
- Express the response magnetic field based on the traveling magnetic field generated by the stator winding.
- Express the force experienced by the rotor into a function based on the traveling magnetic field and obtain the input power, the winding power loss and the eddy current loss with the input voltage, current, the winding resistance and the eddy current density.

- Calculate the corresponding torques based on the force function, the rotor radius, the coulomb friction torque and the viscous friction resistance.
- There are two ways to obtain the output power. One is to multiply the output torque with the rotational speed. The other is to use the input power minus the winding loss, the friction loss and the eddy current loss.
- Compare the output power obtained from two approaches. There is no error on the model derivations if the results are the same.

The analytical model provides the insight about the distribution of the magnetic field and the influence of the harmonics on the motor performance. However, the model has some shortcomings, for example, the model can not show the influence of the higher harmonics. Thus, it is necessary to build a simulation model to compensate. As what mentioned in [15], FEM can easily take into account the complicated geometries and the material properties to overcome the shortcomings of the analytical model.

2.3. Self-inductance and load curve

The ANSYS simulation gives a more realistic result while the analytical model from Mathcad is a good tool to do mathematical analysis such as, the Fourier analysis. Thus, importing the simulation data from ANSYS into the analytical model in Mathcad would be a good approach for analyses. But there are several parameters need to be modified, and the self-inductance is an important one because its value influences the motor performance a lot based on the test in the modeling. Two approaches are used here to obtain the self-inductance value.

The first approach is to get the value from the impedance analyzer. The measurement results is shown in Figure 2.5. It can be seen from the marker that the self-inductance value is 0.802mH under 200Hz. However, the inductance value suffers a quick change due the the frequency changing. That is due to the influence of the response field generated by the eddy current. Thus, the value obtained from the impedance analyzer might not be the accurate self-inductance value of the winding coil.

To remove the influence on the self-inductance value from the eddy current, the conductive layer is removed in the second approach. The current with RMS value of 1A is put in the prototype winding and the waveform of both the voltage and current are obtained. Then the phase angle difference between them is calculated. According to Equation 2.2, the self-inductance value can be obtained.

$$L = \frac{U_{peak} * cos(\theta)}{2 * \pi * f * I_{peak}}, \tag{2.2}$$

where U_{peak} and I_{peak} are the peak values of the voltage and the current; θ is

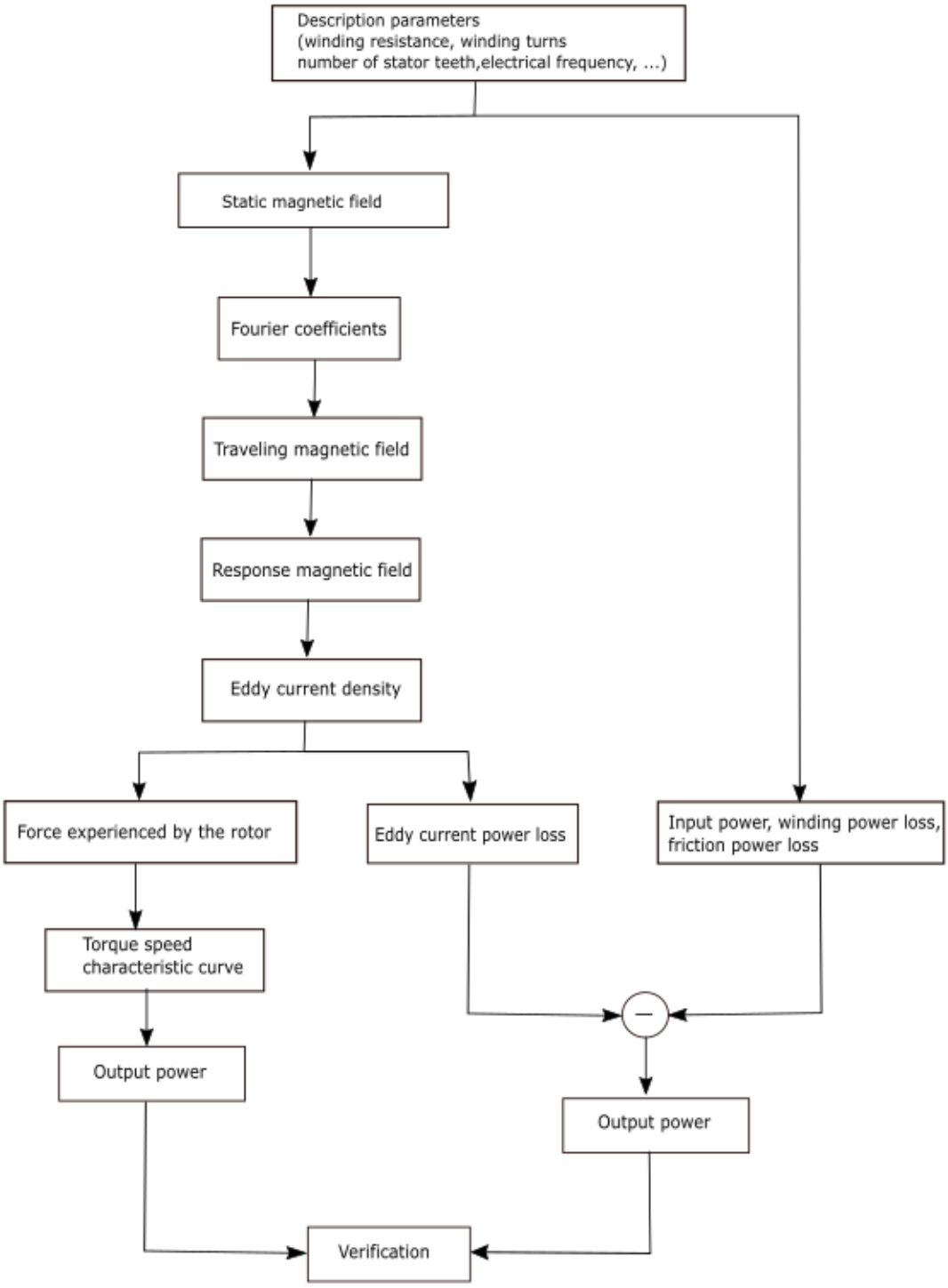

Figure 2.4: Analytical model description flow chart.

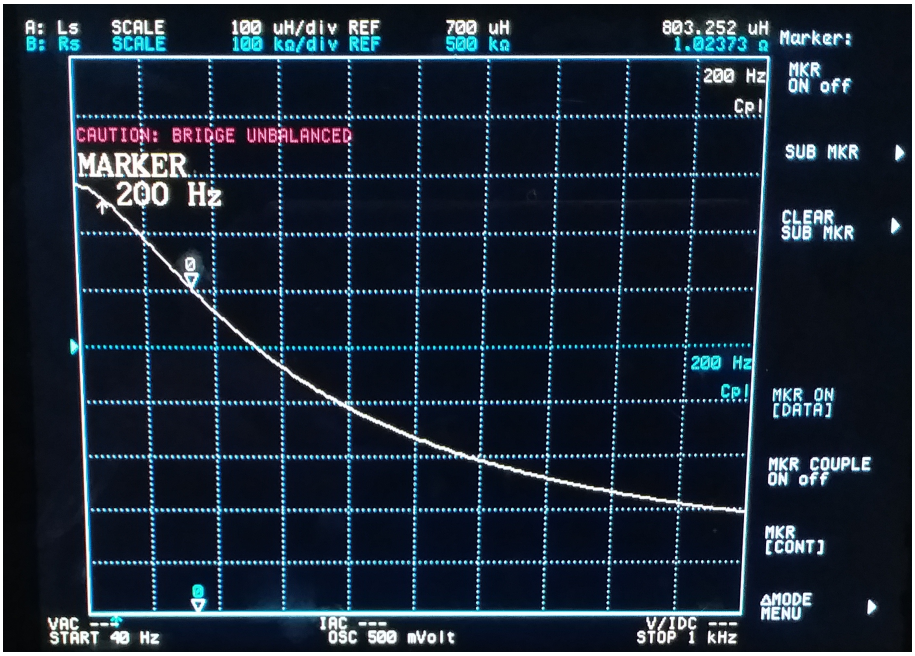

Figure 2.5: Self-inductance measurement for one winding from impedance analyzer.

the phase angle difference and f is the electrical frequency. The calculation results are shown in Table 2.2. It can be seen that under 200Hz, the self-inductance value is around 1.3728 mH. There are some fluctuations on the calculated self-inductance values, which might caused by the inaccuracy of the data reading.

Table 2.2: Self-inductance value under different electrical frequencies.

Frequency (Hz)	40	70	100	160	200
Self-inductance value (mH)	1.3367	1.3577	1.3550	1.3429	1.3278
Frequency (Hz)	250	300	400	500	600
Self-inductance value (mH)	1.3177	1.3359	1.4927	1.4566	1.4204

The self-inductance values obtained from the second approach are larger than the values from the first approach. This is reasonable because the conductive layer is removed in the second measurement and the influence of the response magnetic field does not exist in the second approach anymore. After comparing the self-inductance values from two approaches, 1.3728mH under 200Hz is taken. After the modification of the analytical model, the torque speed characteristic curve shown in Figure 2.6 can be obtained from the modeling.

Having a general understanding of the motor performance is the fundamental to find the solutions. The purpose of the work above is to approach the measurement results shown in Figure 2.3 by modifying the analytical model. The modeling results shown in Figure 2.6 is similar with the measuring results in Figure 2.3.

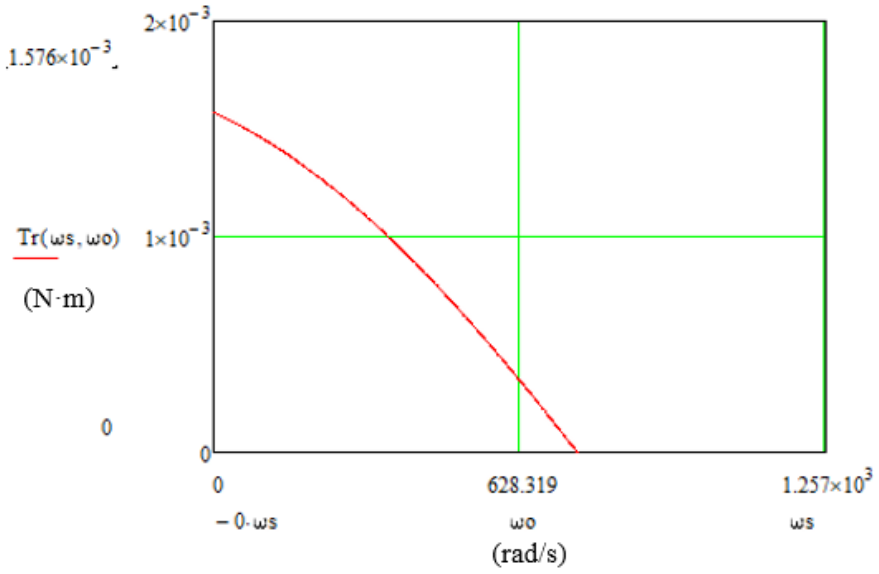

Figure 2.6: Torque speed characteristic curve with magnetic field generated by ANSYS.

2.4. Fourier analysis and harmonic content

Based on the analytical model and the prototype shown in Figure 2.1, an ANSYS simulation model is built as what shown in Figure 2.7. One phase winding out of three is used for study. The magnetic field distribution is shown in Figure 2.8. The waveform of the magnetic field is close to a square wave. To understand the characteristic of the magnetic field, Fourier analysis is performed to get the harmonic coefficients a_i, which are listed in Table 2.3 and i represents the sequence number of the harmonic.

Table 2.3: Harmonic coefficients for the six slots stator magnetic field waveform generated by analytical model.

i^{th} harmonic	1	5	7	11	13
Coefficient ratio a_i/a_1	1	0.254	-0.068	-0.122	4.732×10^{-3}
i^{th} harmonic	17	19	21	23	25
Coefficient ratio a_i/a_1	0.07	0.013	-0.032	-0.039	-0.017

It can be seen from the Table 2.3 that, the 5^{th}, 7^{th}, and 11^{st} harmonics have big harmonic content. That means these harmonics have certain influence on the magnetic field and the motor performance. To verify the influence of the 5^{th}, 7^{th}, and 11^{st} harmonics, these three coefficients are set as zero manually in the modeling. Then the load curve becomes as Figure 2.9, which is much better than what is shown in Figure 2.6. Thus, the assumption can be raised that the 5^{th}, 7^{th}, and 11^{st} harmonics have certain influence on the motor performance.

There are previous studies about the influence on the motor performance due

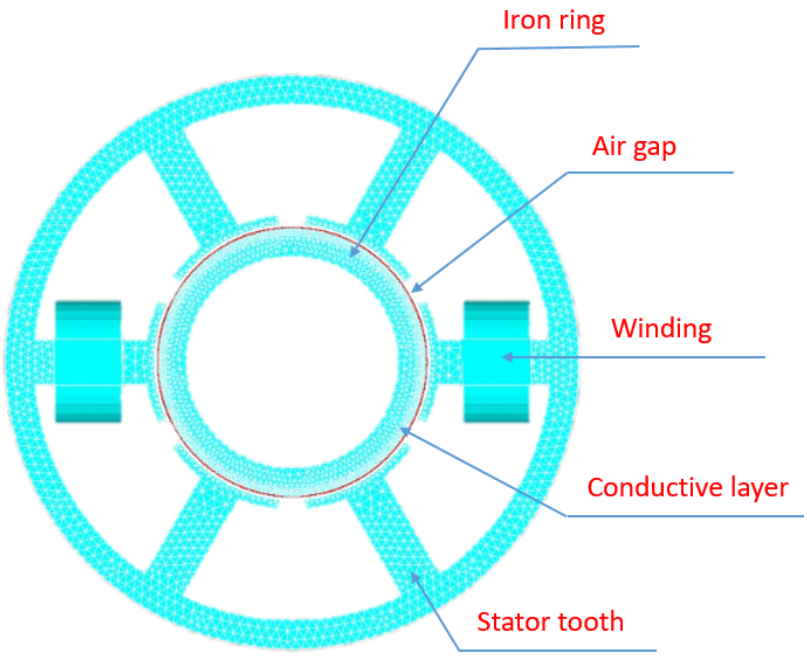

Figure 2.7: ANSYS model with six slots.

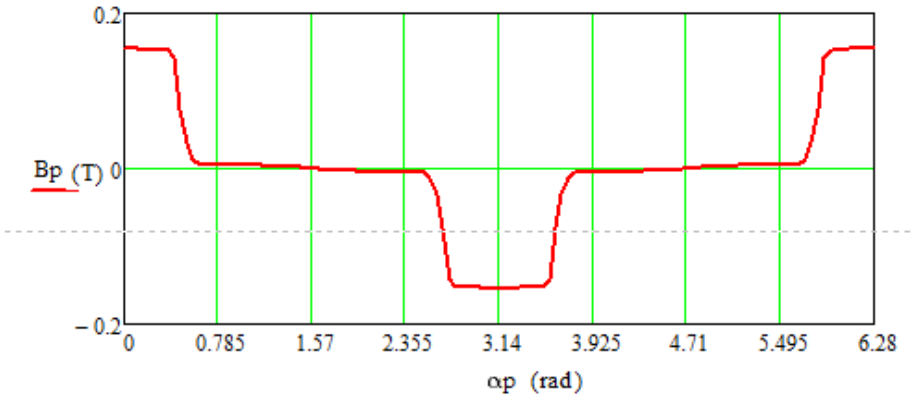

Figure 2.8: Magnetic field generated from analytical model.

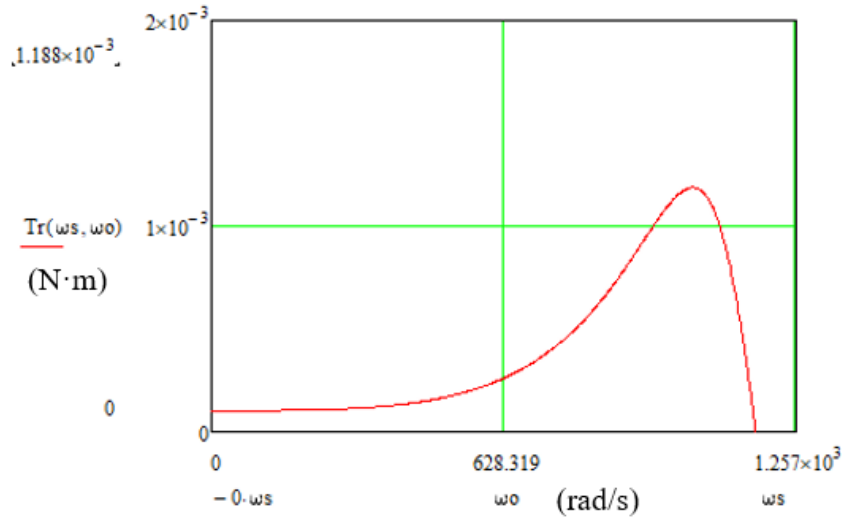

Figure 2.9: Torque speed characteristic curve without 5^{th}, 7^{th}, and 11^{st} harmonics.

to the space harmonics. For example, in [16], harmonic study is conducted for a 72 slots asynchronous motor. The performance of several harmonics are analysed with FEM. In [17], the causes and the origins of the harmonic distortions in a brushless doubly fed induction machine are studied. The research also proposes that applying a different winding configuration can help improve the motor performance. Thus, a proper winding configuration might be the solution.

2.5. Conclusions

This Chapter describes the cause that leads to the problematic motor performance with several tests. In the meanwhile, the analytical model used for study is described in general. It is verified that the 5^{th}, 7^{th}, and 11^{st} harmonics have certain influence on the motor performance after the Fourier analysis on the magnetic field. Then based on the literature studies of the previous work, a proper winding configurations might be a good approach to improve the motor performance.

3

Harmonic elimination

Based on the problem description in Chapter 2, the space harmonics have certain influence on the motor performance. This Chapter proposes the method to suppress the desired harmonics. The method is described with mathematical derivations first. Then the effectiveness of the raised method is verified with modeling and simulation.

3.1. Mathematical verification

Based on the knowledge of Fourier series [18], it is known to all that a periodic real-valued function $f(x)$ can be expressed as Equation 3.1, where x is the distance and λ is the wavelength.

$$f(x) \approx \sum_{n=0}^{n=nh} (a_n cos\frac{2\pi nx}{\lambda} + b_n sin\frac{2\pi nx}{\lambda}), \tag{3.1}$$

where nh is the number of harmonics considered; a_n is the coefficient of the odd function term and b_n is the coefficient of the even function term. One can evaluate the status of certain harmonics with the value of the corresponding harmonic coefficients. Due to the symmetrical structure of the motor, the generated magnetic field can be expressed as an even function $f(\alpha)$ as Equation 3.2 by choosing the proper reference stator teeth and distributing the winding in a symmetrical way.

$$f(\alpha) \approx \sum_{i=0}^{i=nh} a_i cos(i\alpha), \tag{3.2}$$

where α is the mechanical angle shown in Figure 3.1.

The magnetic field $f(\alpha)$ in Equation 3.2 is generated by all the winding turns on stator of one phase winding. If the system can be considered as linear,

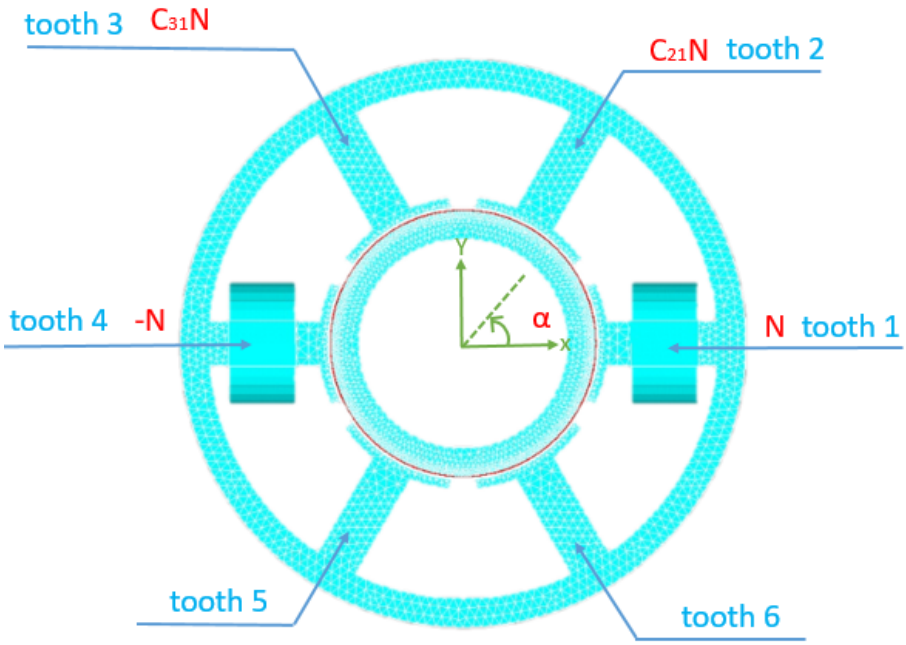

Figure 3.1: Motor quantities illustration.

then the magnetic field $f(\alpha)$ can be considered as the sum of the magnetic field $f_m(\alpha)$ in Equation 3.3, which represents the magnetic field generated by the winding turns on each stator tooth of the chosen phase winding.

$$f_m(\alpha) \approx \sum_{i=0}^{i=nh} C_{m1} a_i' cos(i(\alpha + \frac{2\pi(m-1)}{p})) \quad (m = 1, 2, 3, 4, 5, 6), \tag{3.3}$$

where m is the sequence number of stator tooth; p is the number of the slots. The term $(\alpha + 2\pi m/p)$ represents the location of this tooth compared with the reference, and C_{m1} represents the amplitude change of the magnetic field compared with the reference due to the different number of winding turns.

Based on Figure 3.1, if the tooth 1 is chosen as the reference and there are N winding turns on it, then tooth 4 should also have N turns while in a different direction. The direction of the winding turns which generate the flux into the air-gap is defined as positive while the direction of the winding turns which generate the flux out of the air-gap is defined as negative. They form one phase of the windings out of three. Suppose that there are $C_{21}N$ turns on tooth 2 and $C_{31}N$ turns on tooth 3, where C_{21} and C_{31} are constants. Then C_{21} should equal to C_{31}, because the winding distribution is expected to be

symmetrical. Then the magnetic field can be expressed as Equation 3.4.

$$f_{total}(\alpha) \approx \sum_{i=0}^{i=nh} a_i' cos(i\alpha) + C_{21} a_i' cos(i(\alpha + \frac{\pi}{3}) + C_{31} a_i' cos(i(\alpha - \frac{\pi}{3}) \\ = \sum_{i=0}^{i=nh} a_i' cos(i\alpha)(1 + 2C_{21} cos(i(\frac{\pi}{3})). \tag{3.4}$$

It can be noticed that the relationship between the harmonic coefficient a_i in Equation 3.2 and a_i' in Equation 3.4 is $a_i = a_i'(1+2C_{21}cos(i(\frac{\pi}{3})))$. If the term $1+2C_{21}cos(i(\alpha+3/\pi))$ equals to zero, then the corresponding harmonic coefficient value a_i' is not important anymore, i.e., $a_i = 0$ due to $1+2C_{21}cos(i(\alpha+3/\pi)) = 0$. However, to make this term equal to zero, the constant C_{21} should equal to -1, which means, the winding turns on stator tooth 2 should have N turns as tooth 1 while in the opposite direction. This winding method would lead to the square wave magnetic field distribution similar with Figure 2.8, which will not have good harmonic content as illustrated in Chapter 2. Thus, the solution is not reasonable for this case. However, it can be noticed from this trial that the number of the terms in Equation 3.4 depends on the number of stator slots. So increasing the number of stator slots might lead to other solutions.

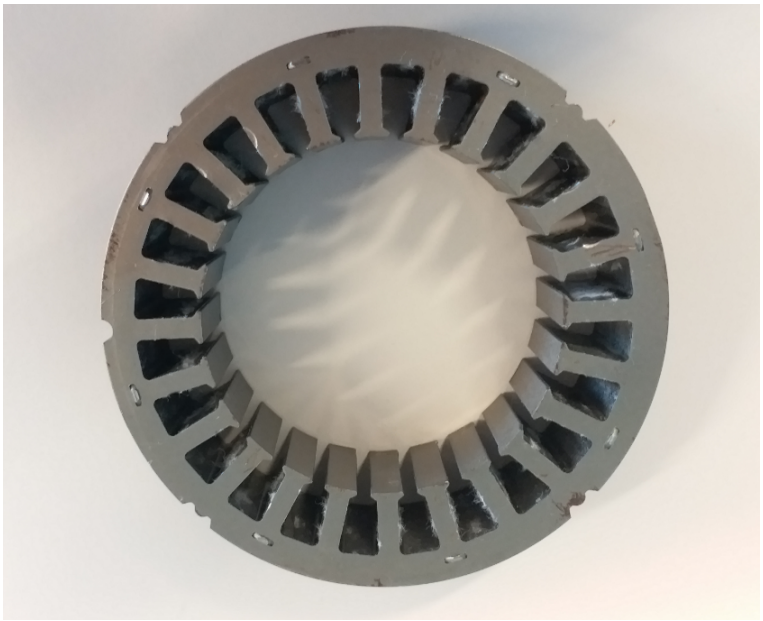

Figure 3.2: 24-slot stator.

This is a three phase motor, which means that there are three group of winding in total. The number of stator teeth enclosed by each phase winding should be the same. Thus, the number of stator slots should be the multiple of 3. At the same time, one phase winding is divided into two equal parts to generate the flux in the opposite direction. Thus the number of stator teeth,

which equals to the number of slots, should also be a multiple of 2. Then in general, the number of stator slots should be a multiple of 6. Except 6 tried above, 12, 18, 24,... can be used.

There are no strict rules in choosing the number of stator slots. It depends on the desired motor weight, cost and operating characteristics [19]. In industries, the number of slots depends on lots of factors and requirements. There are studies such as [20] and [21], which reveals the influence on the motor performance due to different stator slots, number of poles and etc.. In the research, 24 slots stator is already available as a prototype shown in Figure 3.2. Thus 24 slots stator is chosen as an example to solve the problem.

According to the method raised above, the magnetic field generated by the 24 slots stator with one winding can be expressed as Equation 3.5.

$$\begin{aligned} f_{total}(\alpha) \approx & \sum_{i=0}^{i=nh} a_i' cos(i\alpha) + C_{21}a_i' cos(i(\alpha + \frac{\pi}{12}) + C_{31}a_i' cos(i(\alpha + \frac{\pi}{6}) \\ & + C_{41}a_i' cos(i(\alpha + \frac{\pi}{4}) + C_{51}a_i' cos(i(\alpha + \frac{\pi}{3}) + C_{61}a_i' cos(i(\alpha + \frac{5\pi}{12}) \\ & + C_{71}a_i' cos(i(\alpha - \frac{5\pi}{12}) + C_{81}a_i' cos(i(\alpha - \frac{\pi}{3}) + C_{91}a_i' cos(i(\alpha - \frac{\pi}{4}) \\ & + C_{101}a_i' cos(i(\alpha - \frac{\pi}{6}) + C_{111}a_i' cos(i(\alpha - \frac{\pi}{12}) \\ = & \sum_{i=0}^{i=nh} a_i' cos(i\alpha)(1 + 2C_{21}cos(i(\frac{\pi}{12}) + 2C_{31}cos(i(\frac{\pi}{6}) \\ & + 2C_{41}cos(i(\frac{\pi}{4}) + 2C_{51}cos(i(\frac{\pi}{3}) + 2C_{61}cos(i(\frac{5\pi}{12})). \end{aligned} \tag{3.5}$$

Equation 3.5 can be sorted into matrix form. Matrix A and vector V can be defined as follows. The i_1 to i_5 in A matrix are the sequence number of the harmonics which desired to be eliminated.

$$A = \begin{bmatrix} cos(i_1(\frac{\pi}{12}) & cos(i_1(\frac{\pi}{6}) & cos(i_1(\frac{\pi}{4}) & cos(i_1(\frac{\pi}{3}) & cos(i_1(\frac{5\pi}{12}) \\ cos(i_2(\frac{\pi}{12}) & cos(i_2(\frac{\pi}{6}) & cos(i_2(\frac{\pi}{4}) & cos(i_2(\frac{\pi}{3}) & cos(i_2(\frac{5\pi}{12}) \\ cos(i_3(\frac{\pi}{12}) & cos(i_3(\frac{\pi}{6}) & cos(i_3(\frac{\pi}{4}) & cos(i_3(\frac{\pi}{3}) & cos(i_3(\frac{5\pi}{12}) \\ cos(i_4(\frac{\pi}{12}) & cos(i_4(\frac{\pi}{6}) & cos(i_4(\frac{\pi}{4}) & cos(i_4(\frac{\pi}{3}) & cos(i_4(\frac{5\pi}{12}) \\ cos(i_5(\frac{\pi}{12}) & cos(i_5(\frac{\pi}{6}) & cos(i_5(\frac{\pi}{4}) & cos(i_5(\frac{\pi}{3}) & cos(i_5(\frac{5\pi}{12}) \end{bmatrix}.$$

$$V = \begin{bmatrix} C_{21} \\ C_{31} \\ C_{41} \\ C_{51} \\ C_{61} \end{bmatrix}.$$

To make the term $1+2C_{21}cos(i(\frac{\pi}{12})+2C_{31}cos(i(\frac{\pi}{6})+2C_{41}cos(i(\frac{\pi}{4})+2C_{51}cos(i(\frac{\pi}{3})+2C_{61}cos(i(\frac{5\pi}{12})$ equals to zero, A*V should equal to -1/2. Suppose $i_1 = 5, i_2 = 7, i_3 = 11, i_4 = 13, i_5 = 17$. Then A matrix can be calculated as

$$A = \begin{bmatrix} 0.259 & -0.866 & -0.707 & 0.5 & 0.966 \\ -0.259 & -0.866 & 0.707 & 0.5 & -0.966 \\ -0.966 & 0.866 & -0.707 & 0.5 & -0.259 \\ 0.259 & -0.866 & -0.707 & 0.5 & 0.966 \\ 0.966 & 0.866 & 0.707 & 0.5 & 0.259 \end{bmatrix}.$$

However, the determinant of matrix A, |A|, under this circumstance is zero, which means vector V can not be obtained by calculating the inverse of A matrix.

During the tests, it is found that the 19^{th} harmonic is small while the 5^{th} got suppressed. If the 7^{th} harmonic is suppressed then the 17^{th} harmonic is also small, and if the 23^{rd} harmonic got suppressed, the fundamental harmonic becomes very small. Thus, there is a corresponding relation for the two harmonics of which the sum is the number of stator slots. For example, for a 12 slots motor, if the 5^{th} harmonic is suppressed then the 7^{th} is small as well. Due to 5 plus 7 is the number of motor slots, 12.

One condition for the matrix to be reversible is that all the equations form by this matrix should be independent. Because there is a corresponding relation between two harmonics, then these two harmonics can not be put into the matrix in Equation 3.3 at the same time. That also explains the reason why in Equation 3.3, the matrix is irreversible when the 5^{th}, 7^{th}, 11^{st}, 13^{rd} and 17^{th} harmonics are put together at the same time. Because the 7^{th} and the 17^{th} are related.

Since the most desirable harmonics to suppress are the 5^{th}, 7^{th} and 11^{st}, the size of A matrix is reduced to three by three. A three by three matrix is enough to suppress three harmonics at the same time while a reversible matrix can be got.

Then Equation 3.5 should be changed into Equation 3.6, and the harmonic coefficient a_i in Equation 3.2 should be $a_i = a_i'(1+2C_{21}cos(i(\frac{\pi}{12})+2C_{31}cos(i(\frac{\pi}{6})+2C_{41}cos(i(\frac{\pi}{4}))))$.

$$f_{total}(\alpha) \approx \sum_{i=0}^{i=nh} a_i' cos(i\alpha)(1 + 2C_{21}cos(i(\frac{\pi}{12}) + 2C_{31}cos(i(\frac{\pi}{6}) + 2C_{41}cos(i(\frac{\pi}{4})). \tag{3.6}$$

Sort Equation 3.6 into the matrix form. Matrix A can be expressed as follows and it is a reversible matrix.

$$A = \begin{bmatrix} cos(i_1(\frac{\pi}{12}) & cos(i_1(\frac{\pi}{6}) & cos(i_1(\frac{\pi}{4}) \\ cos(i_2(\frac{\pi}{12}) & cos(i_2(\frac{\pi}{6}) & cos(i_2(\frac{\pi}{4}) \\ cos(i_3(\frac{\pi}{12}) & cos(i_3(\frac{\pi}{6}) & cos(i_3(\frac{\pi}{4}) \\ cos(i_4(\frac{\pi}{12}) & cos(i_4(\frac{\pi}{6}) & cos(i_4(\frac{\pi}{4}) \\ cos(i_5(\frac{\pi}{12}) & cos(i_5(\frac{\pi}{6}) & cos(i_5(\frac{\pi}{4}) \end{bmatrix}. = \begin{bmatrix} 0.259 & -0.866 & -0.707 \\ -0.259 & -0.866 & 0.707 \\ -0.966 & 0.866 & -0.707 \end{bmatrix}.$$

By calculating the inverse matrix of A under the condition that A*V=-1/2, vector V can be obtained as

$$V = \begin{bmatrix} 0.816 \\ 0.577 \\ 0.299 \end{bmatrix}.$$

The physical meaning of vector V is that, compared with the reference stator tooth which has N winding turns, the first pair of side teeth should have 0.816N winding turns; the second pair of side teeth should have 0.577N winding turns and the third pair of side teeth should have 0.299N turns. It is also interesting to be found that in A matrix, 0.259, 0.866. 0.707 are the sin values of 15°, 45°, 60°. The relation between the values in the matrix and the mechanical angle for the winding distribution can be studied in the future.

All the mathematical derivation are shown above to calculated the winding distribution which can help suppress the $5^{th}, 7^{th}$ and 11^{st} harmonics. Modeling and simulation are presented in the follows to verify this winding configuration.

3.2. Simulation and modeling

The analytical model and simulation are used in this section to verify the effectiveness of the winding scheme raised in section 3.1. Besides, some details such as the data processing method in the simulation are described.

3.2.1. Analytical modeling

By putting the winding turns distribution into analytical model based on vector V in Equation 3.1, Figure 3.3 is the result of the magnetic field waveform, where $f(\alpha)$ is the function value of the Fourier series and α is the electrical angle within one period. In this research, the electrical angle also equals to the mechanical angle. Compared with Figure 2.8, the magnetic waveform under this winding configuration is closer to sinusoidal wave. To know the harmonic content, Fourier analysis is conducted and the harmonic coefficient ratios are shown in Table 3.1.

It can be seen from Table 3.1 that the $5^{th}, 7^{th}$ and 11^{st} harmonic coefficient ratios are close to zero, which illustrates the effectiveness of this winding distribution scheme from the analytical model aspect. However, to reflect the

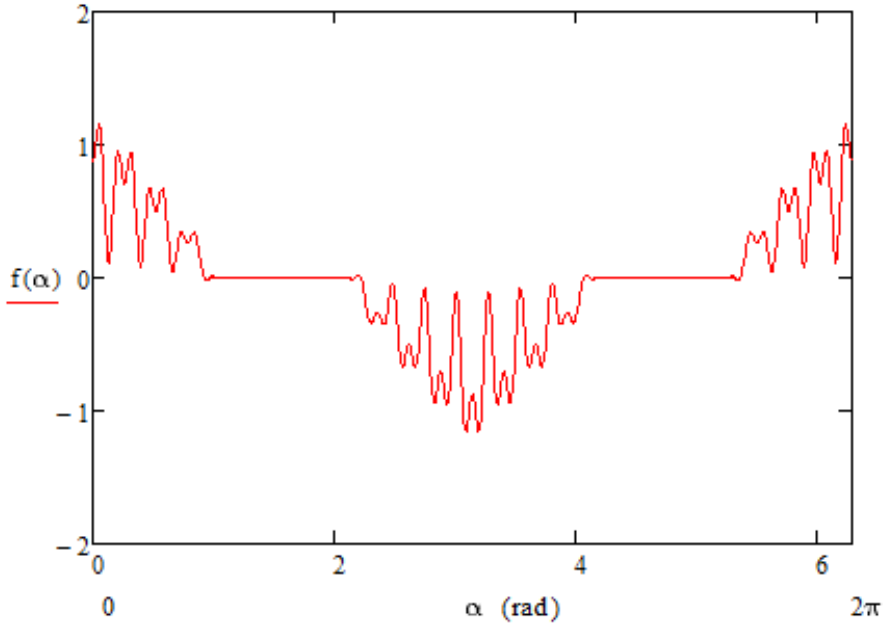

Figure 3.3: Magnetic field distribution for one phase winding from Mathcad model with 24-slot stator.

Table 3.1: Harmonic coefficients for magnetic field distribution from Mathcad model with 24 slots stator.

i^{th} harmonic	1	5	7	11	13
Coefficient ratio a_i/a_1	1	7.007×10^{-13}	-2.131×10^{-13}	9.573×10^{-14}	8.667×10^{-14}
i^{th} harmonic	17	19	23	25	
Coefficient ratio a_i/a_1	-1.28×10^{-13}	3.377×10^{-13}	0.278	0.191	

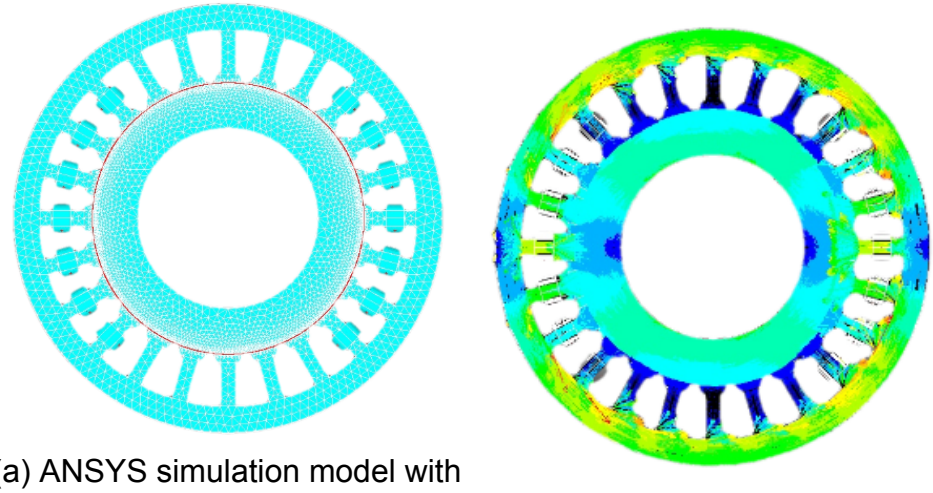

(a) ANSYS simulation model with 24-slot stator and designed winding scheme.

(b) Vector plot of the magnetic field from ANSYS simulation

Figure 3.4: ANSYS simulation for 24-slot motor.

real influence of the higher harmonics and verify the winding scheme further, a simulation model is needed.

3.2.2. ANSYS simulation modeling

The simulation model is built in the software ANSYS as Figure 3.4a and the simulation vector plot of the magnetic field is shown as Figure 3.4b. Except the two reference stator teeth in the middle at two sides, there are three pairs of side teeth on each side with the winding ratio derived from section 3.1. The purpose of the simulation is to get the magnetic field generated by the stator winding and analysis the corresponding harmonic content. Thus, the analyses is static and the influence of the rotor parts are not included.

After building the simulation model, a circular path is chosen at the middle of the conductive layer to collect the magnetic field data. With FEM, the model is meshed into lots of elements, including this path. Every element has several nodes, and the magnetic field on x and y direction for every node can be obtained with the APDL command '*get,Bxx,node,NodeNr,B,x' and '*get,Byy,node,NodeNr,B,y' in ANSYS. Figure 3.5 shows an example for the element in yellow slash. The magnetic field on the three nodes of this element can be obtained as B_{xxn} and B_{yyn} for the n^{th} node. These nodes all belong to one element. Thus, all the B_{xxn} and B_{yyn} of this element are added together in x and y direction as B_x and B_y. To get the magnetic field value at the radial direction, which is represented as B_r, a transformation between B_r, B_x and B_y is made as Equation 3.7. Also, to get the average value for one element, the sum is divided by the number of the nodes N_{node} on this element.

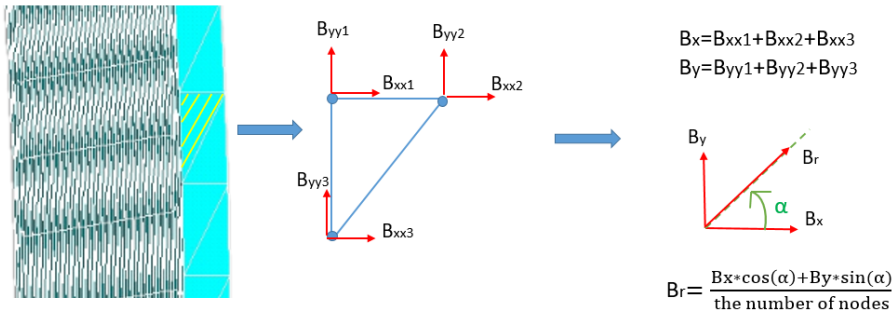

Figure 3.5: Magnetic field data calculation method for elements on the path of conductive layer.

$$B_r = \frac{\sum_{n=0}^{n=N_{node}} (B_{xxn} cos(\alpha) + B_{yyn} sin(\alpha))}{N_{node}} = \frac{B_x cos(\alpha) + B_y sin(\alpha)}{N_{node}} \tag{3.7}$$

The step length of the collected data is set as 3°, which means 120 data in total are collected for 360°, and the angle is represented by α in Figure 3.5 and in Equation 3.7. α indicates the angle difference between the current position compared with the x axial on the working plane, which is also shown in Figure 3.1. After getting all the 120 data, they are plotted in Figure 3.6.

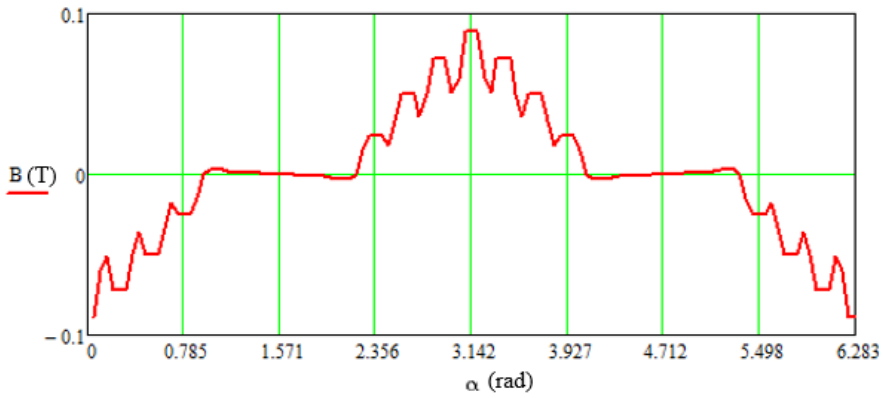

Figure 3.6: Magnetic field distribution on conductive layer path for one phase winding from ANSYS simulation results.

Compared with Figure 3.3, the differences between modeling and simulation results can already be noticed. The analytical model describes a very ideal situation. There is no magnetic flux under the stator teeth without winding turns. While it is not the case in ANSYS simulation. What is shown in Figure 3.6 is closer to reality. With the magnetic flux density data from ANSYS sim-

ulation results, the harmonic content can be obtained with Fourier analysis as shown in Table 3.2.

Table 3.2: Harmonic coefficients for magnetic field distribution from ANSYS simulation with 24 slots stator

i^{th} harmonic	1	5	7	11	13
Coefficient ratio a_i/a_1	1	-1.291×10^{-3}	-1.792×10^{-3}	-1.615×10^{-3}	1.242×10^{-4}
i^{th} harmonic	17	19	23	25	
Coefficient ratio a_i/a_1	9.748×10^{-4}	8.559×10^{-4}	0.056	0.02	

From Table 3.2, it can be seen that the $5^{th}, 7^{th}$ and 11^{th} harmonic coefficients are still small and compared with Table 3.1, the 23^{rd} and 25^{th} harmonic are smaller. The simulation better reflects the influence of higher harmonics and the effectiveness of this winding scheme is also proved by the ANSYS simulation.

3.3. Further exploration

In this section, a 12-slot stator is used as a media to design a well-performing winding distribution for the 24-slot stator while achieving a different flux direction.

First, a 12-slot stator is considered. Based on the scheme shown in Chapter 2. Equation 3.8 can be got as a profile function to describe the magnetic field distribution. Make $1 + 2C_{21}cos(i(\frac{\pi}{12}) + 2C_{31}cos(i(\frac{\pi}{6}) = 0$ and sort it into matrix. A matrix and V vector can be got.

$$f_{total}(\alpha) \approx \sum_{i=0}^{i=nh} a_i' cos(i\alpha)(1 + 2C_{21}cos(i(\frac{\pi}{12}) + 2C_{31}cos(i(\frac{\pi}{6})). \tag{3.8}$$

$$A = \begin{bmatrix} cos(i_1(\frac{\pi}{6}) & cos(i_1(\frac{\pi}{3}) \\ cos(i_2(\frac{\pi}{6}) & cos(i_2(\frac{\pi}{3}) \end{bmatrix}.$$

$$V = \begin{bmatrix} C_{21} \\ C_{31} \end{bmatrix}.$$

Set $i_1 = 3$ and $i_2 = 5$. Then based on the equation $A * V = -1/2$, C_{21} is solved as 0.866 and C_{31} is solved as 0.5. Then the one phase winding distributions can be visualized as Figure 3.7. The cross and dot symbol represent the current direction which goes into the paper and goes out of the paper. The directions of the magnetic flux generated by the winding on two reference teeth are indicates by the blue arrows. The direction of the winding turns which generate the flux into the air-gap is defined as positive while the direction of the winding turns which generate the flux out of the air-gap is defined as negative.

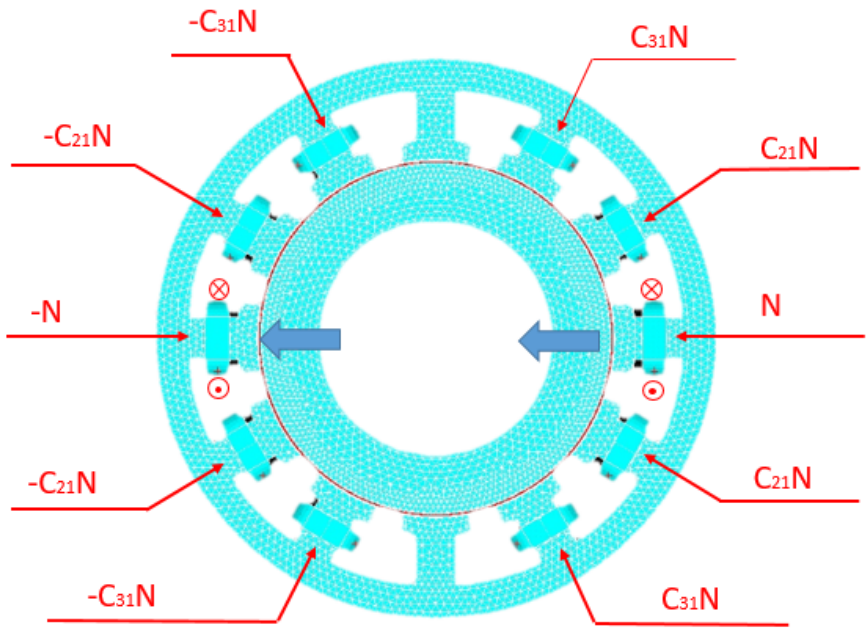

Figure 3.7: One phase winding and flux direction of 12-slot 2 poles motor.

Putting the design into the analytical model, the magnetic field distribution is obtained as Figure 3.8. The corresponding harmonic coefficients are all zero except the fundamental one and the 11^{th}.

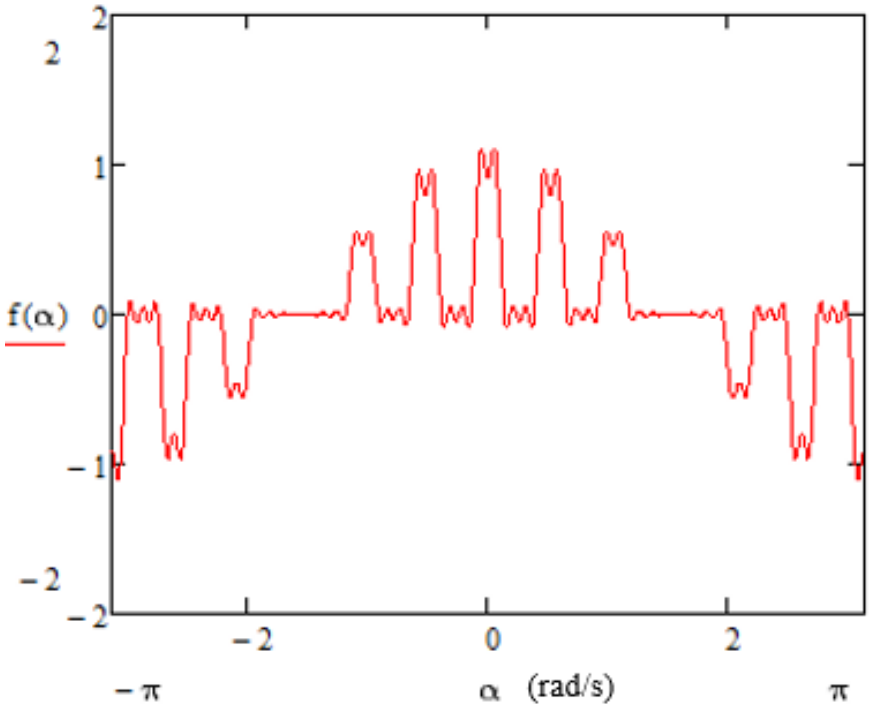

Figure 3.8: Magnetic field distribution for 12 slots motor.

By building the simulation model in ANSYS, it can be found that the 11^{th} harmonic does not have big influence on the motor performance. The torque speed characteristic is shown in Figure 3.9, which indicates the performance is good.

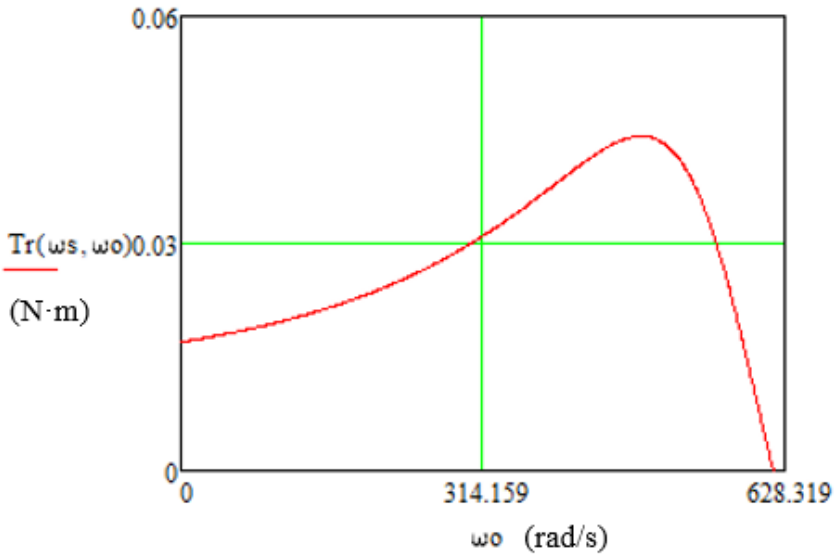

Figure 3.9: Torque speed characteristic curve for 12-slot motor.

With the well-performing winding distribution for 12-slot stator, by putting two of them together, the winding distribution for 24-slot stator can be obtained as Figure 3.10. Compared with Figure 3.4a under the same external conditions, the winding configuration in Figure 3.10 has 4 poles and it would generate more torque while make the mechanical frequency to be half of the electrical frequency. The purpose of the further exploration is to show that by using 12-slot as a unit, the method proposed above can effectively design a well-performing winding configuration for 24-slot stator to make the motor has different characteristics.

3.4. Conclusions

In this chapter, a method to suppress certain harmonics by calculating the winding distribution is proposed. This method is described with the mathematical derivations and the effectiveness is verified with both analytical model from Mathcad and the simulation model from ANSYS. This method is intuitive and it gives the support to design a reasonable winding configuration.

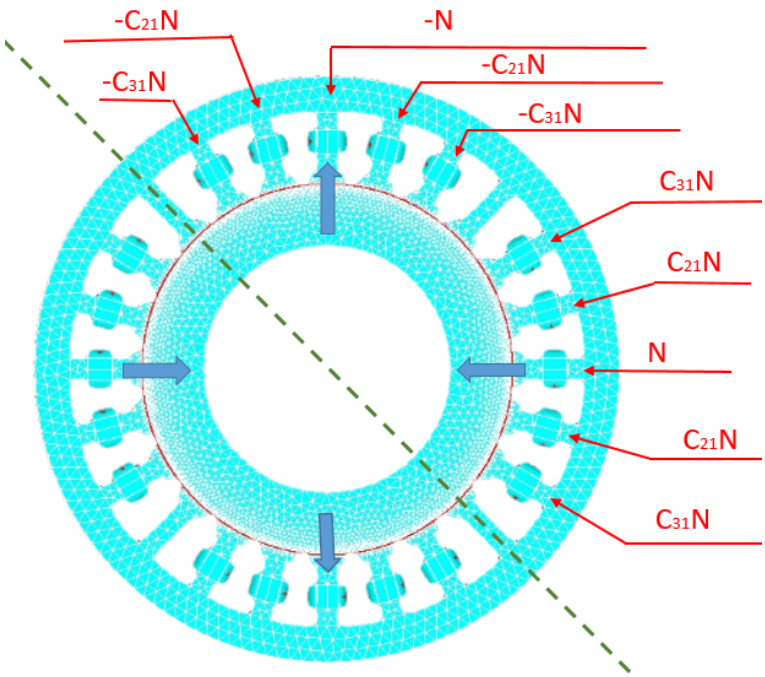

Figure 3.10: One phase winding distribution and flux direction for a 24-slot 4 poles motor.

4

Winding scheme and magnetic field measurement

Chapter 3 raises the harmonic elimination method with certain winding configuration. How to realize the winding distribution into prototype is discussed in this chapter. The previous studies about concentrated and distributed winding, full pitch and short pitch methods are studied first. Then some comparisons between those methods are presented. In the end, the chosen winding configuration is realized into the prototype.

4.1. Classical winding distribution scheme

In this section, some classical winding methods are studied and described, including the concentrated winding, distributed winding, short pitch and full pitch. The advantage and disadvantage of the methods are given and they are compared with the methods used in this research.

4.1.1. Concentrated and distributed windings

In concentrated windings, the coils are concentrated at one slot under one armature pole as what is shown in Figure 4.1. The total emf is the summation of all the emf generated on each coil side.

The characteristic is that all the coil sides of one phase are concentrated in a particular slot under a given pole, i.e., the number of the armature poles equal to the number of the armature slots. The advantage of the concentrated winding is that it can generate large emf compared with other schemes. The disadvantage is that the generated emf waveform is not close to sinusoidal enough. For the motors which desires to have a sinusoidal output waveform, concentrated winding might not be the best choice.

On the opposite of concentrated winding, the distributed winding, as shown in Figure 4.2, are placed in several slots. The advantage is that the emf waveform

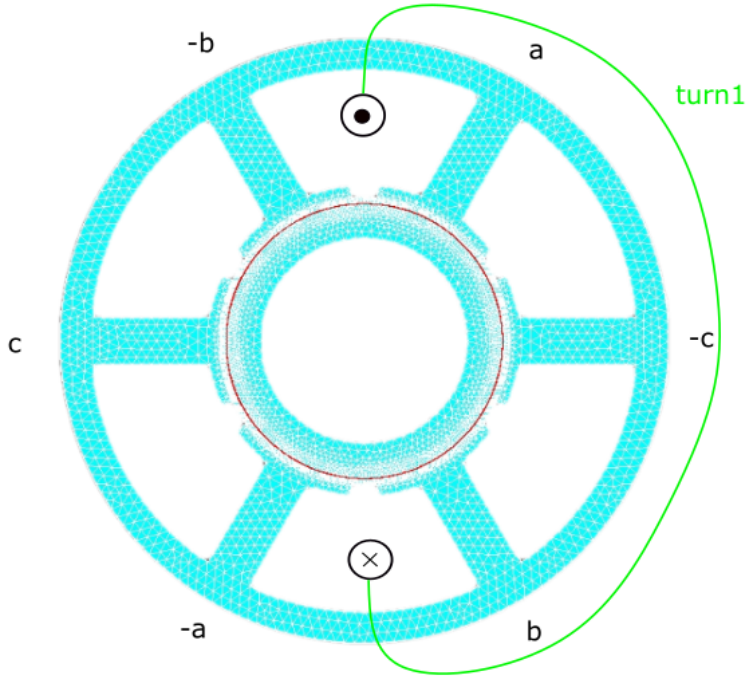

Figure 4.1: Concentrated winding scheme.

generated by the distributed winding is usually closer to sinusoidal wave. Thus it reduces the harmonic emf. At the same time, the even distribution of coils also helps in motor cooling. However, the total emf generated by the distributed winding is not as large as concentrated winding. To reach the same emf level, more winding turns are needed.

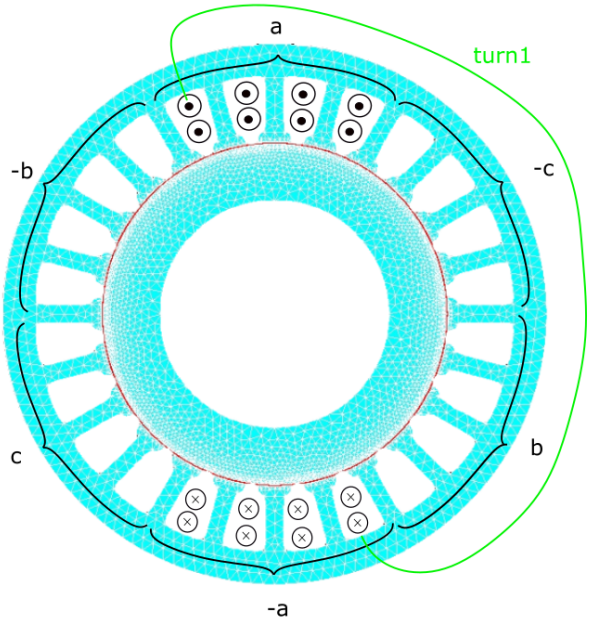

Figure 4.2: Distributed full-pitch winding in a three phase 24 slots motor.

4.1.2. Short pitch and full pitch

Figure 4.2 describes a two pole, three phase full-pitch winding. The distance between two sides of all the individual coils is 180 degrees, which is also called full pole pitch. For example, turn1 in the figure is one coil turn of one phase. The two sides of this coil span 180 electrical degrees. One can imagine that for motors with large radius, the full pitch scheme would costs lots of coil wires to travel from one side to the other.

On the other hand, if two sides of the coil span less than 180 degree, then it is called short pitch (fractional pitch) as shown in Figure 4.3. The two sides of turn1 only span 150 degrees, i.e., 5/6 pitch. Compared with the full pitch winding scheme, short pitch has the advantage in shortening the end connections.

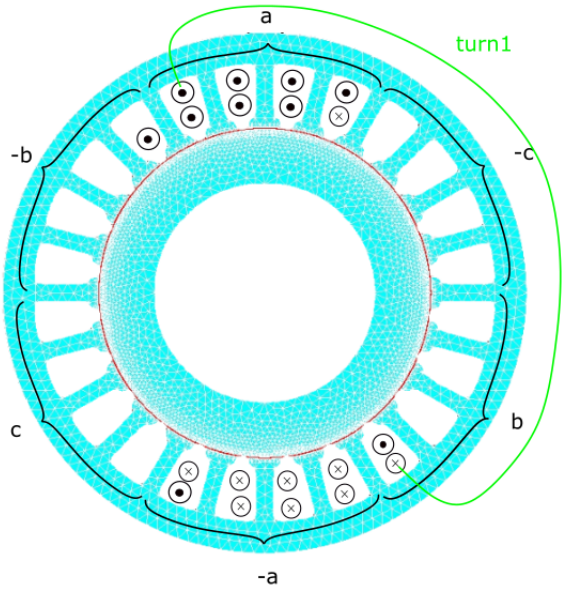

Figure 4.3: Distributed short-pitch winding in a three phase 24 slots motor.

Research [23] has revealed the advantages and the disadvantages of applying the short pitch and full pitch winding configurations in the asynchronous motor with finite element analysis. It shows more harmonic components involved in full pitch leading to the distortion in the sine wave while the situation in short pitch is better.

In general, concentrated full-pitch winding has the superiority of large emf with less winding turns while distributed short-pitch winding has the advantage of better sinusoidal output. Concentrated short pitch winding has the shortcoming of the space harmonic which leads to the considerable eddy-current losses in the conductive layer parts [24]. Each method has its advantages and disadvantages. Thus, the choice should be made base on the motor characteristics and requirements.

In this research, harmonic is the mainly problem and the purpose is to sup-

press certain harmonics to improve the motor performance. Thus, the distributed short pitch winding is more suitable. In the following section, different scheme of the distributed short pitch winding are discussed and compared.

4.2. Comparison between different winding methods

In this section, the stator teeth wound by coil turns, which is represented by using rectangle bars are plotted in the following figures to illustrate the winding distribution. The red numbers represent the number of coil turns in the slots. The positive and negative sign of the number represent the direction of the current in the coil turns, corresponding with the dot and the cross sign. The blue numbers represent the needed effective coil turns to enclose the stator teeth.

During the nowadays automatic process, equal number of turns per slot is commonly used and by distributing in a wise way, a sinusoidal output could be achieved. For example, in Figure 4.4, the number of turns in each slot are 9 turns. The generated waveform is close to sinusoidal wave and it may also have good effects on harmonic elimination. However, it can also be noticed that outside coil turns need to enclose lots of stator teeth, which increases the dissipation in long wires while not contributing to the magnetic field.

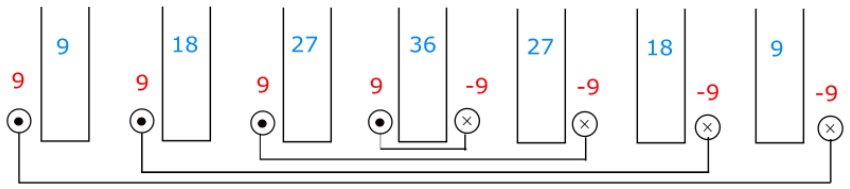

Figure 4.4: Distributed short-pitch winding with equal number of turns per coil.

The purpose of the chosen winding scheme here should be effective in verifying the correctness of the method raised in Chapter 3. The winding scheme should satisfy the requirements, i.e., except the two reference teeth, three side teeth pairs should be included and the winding turns ratio for each pair of the teeth has been determined, i.e., 0.816, 0.577 and 0.299. But in practical, to make sure that the number of winding turns are all integers, the ratio is adjusted to 0.8387, 0.5806, 0.2903, as shown in the illustration figures. Then the coil turns ratio is converted to the number of turns on each tooth represented by the blue numbers in the figures.

The winding requirements raised in Chapter 3 can be realized as in Figure 4.5. The advantage of this winding method is that for the given phase windings, no flux get compensated in the slots due to the opposite direction of the current, i.e., there is only one current direction in every slot. However, it can be noticed that for the outer coils, it needs to enclose seven stator teeth. The

long traveling distance would costs more copper wires and it also increases the difficulties to realize by hands.

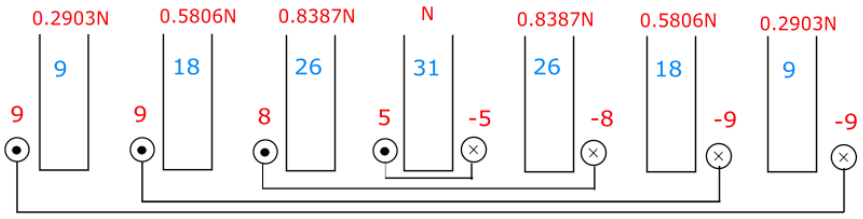

Figure 4.5: Distributed short-pitch winding with unequal number of turns per coil.

To shorten the coil end distance, the number of the enclosed stator teeth is reduced. In Figure 4.6, two stator teeth enclosed in one winding turn. It can be seen that if enclose the stator teeth from left to right as Figure 4.6a, to make the last tooth have enough winding turns, three more turns need to be added individually. If start the winding from two side teeth to the middle as Figure 4.6b, three turns need to be removed from the reference tooth, which is not convenient in practice.

Instead of enclosing two teeth, Figure 4.7 shows the scheme of enclosing three teeth within one winding turn. Figure 4.7a is the illustration to wind the stator teeth from left to right. Also to make sure the last tooth has enough winding turns, 5 more turns need to be added individually. For the scheme of starting winding from two sides teeth to the middle as Figure 4.6, 5 more turns need to be added on the reference tooth. For the above proposed scheme, Figure 4.6a has 39 ineffective turns. Figure 4.6b has 42 ineffective turns. Figure 4.7a has 18 ineffective turns and Figure 4.7b also has 18 ineffective turns. But consider the possible overlapping on the side teeth from other phases, Figure 4.7b is chosen because it has the minimum ineffective turns, i.e., more effective flux and it is more feasible to realize.

Except the scheme listed above, there are more winding method. However, there are always trade off between different methods. Either they generate large emf but cost more winding wires, or saving the winding wires but with small emf. The choice should be made based on the radius, the height of the motor, and the requirements. The prototype in this research is wound by hands and the aim is to verify the effectiveness of the method raised in Chapter 2. The scheme shown in Figure 4.7b has more effective turns than Figure 4.6. The usage of the copper wire and the hand making difficulties are acceptable. Thus, the winding scheme shown in Figure4.7b is chosen.

4.3. Prototype realization

With the winding method in Figure4.7b, copper wires with 0.476mm and 0.5mm diameters are tried as shown in Figure 4.8. Considering the winding overlap, the copper wire with 0.476 mm is chosen. It should be noted

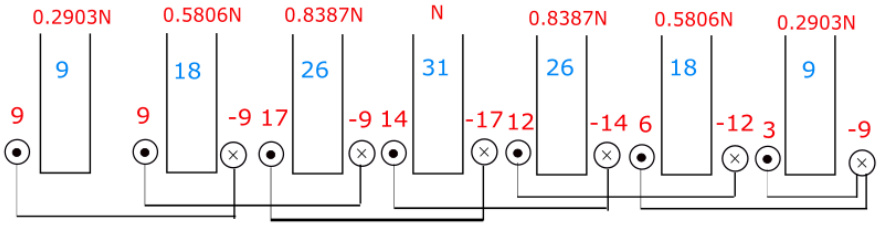

(a) Coils enclose teeth from clockwise direction.

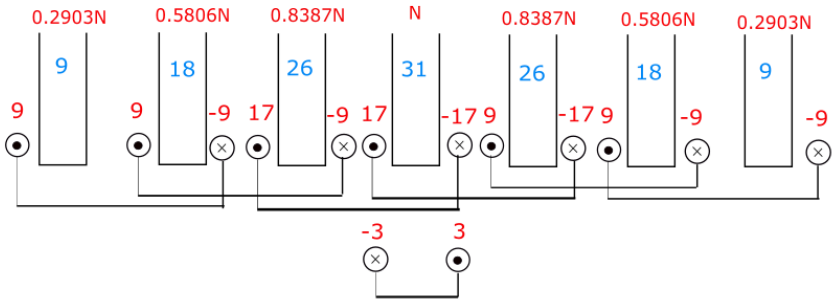

(b) Coils enclose teeth from two sides to middle.

Figure 4.6: Winding scheme for two teeth enclosed in one winding turn.

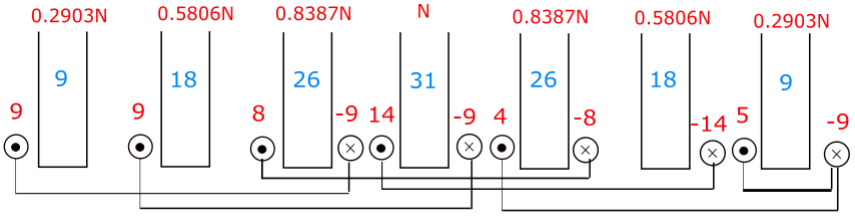

(a) Coils enclose teeth from clockwise direction.

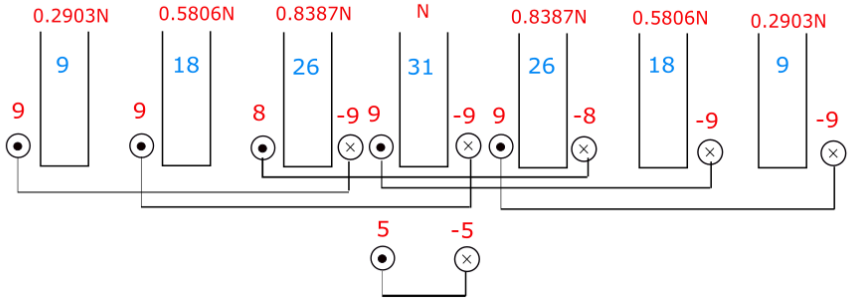

(b) Coils enclose teeth from two sides to middle.

Figure 4.7: Winding scheme for three teeth enclosed in one winding turn.

that because the winding is made by hands, the utilization of slots space is not very effective. With machinery making, thicker wire could be used and the number of turns could be increased.

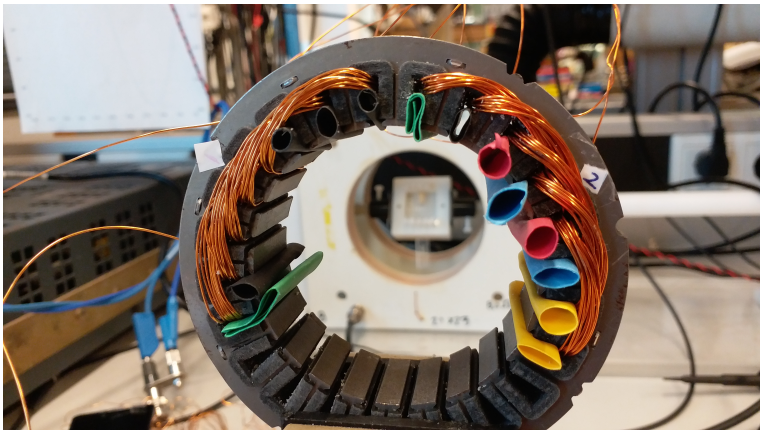

Figure 4.8: Winding trial with two different diameters copper wire.

The complete three phase winding stator is shown in Figure 4.9. The stator and copper wires are isolated with black plastic covers to prevent the short circuit between iron stator and copper wire. The windings are fixed with high tenacity white nylon wire. One winding is made into two half separately. They can be connected into series to generated flux in the opposite direction. The average resistance for half winding is around 0.67175Ω.

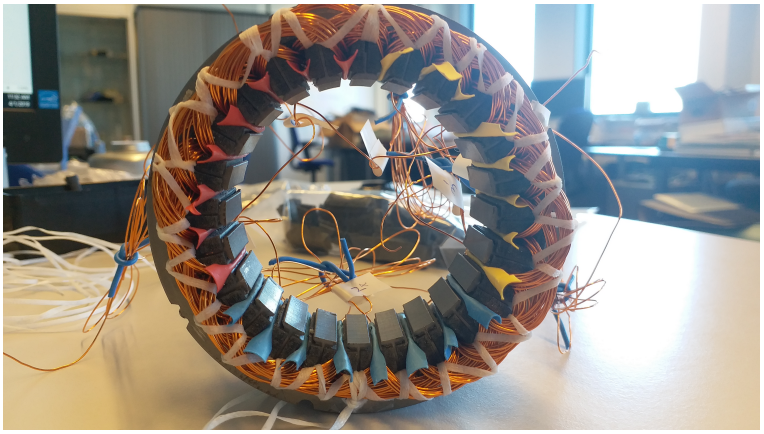

Figure 4.9: 24 slots stator with fixed three phase winding.

4.4. Magnetic field measurement

The magnetic field from modeling and simulation are presented in Chapter 3. It is interesting to measure the real magnetic field generated by the windings. Figure 4.10 is the set up to measure the magnetic field. The device used to measure the magnetic field strength is called Gauss meter. The sensor of the Gauss meter is put into the air gap between the stator and rotor. The display

data is collected under every tooth and slot by slowly rotating the stator. Because the sensor of the Gauss meter is very delicate, the measurement can only be conducted while the motor is standing. Thus, 1A DC current is put through the winding and the three phase windings are measured separately. Figure4.11 are the plots of the measurement results.

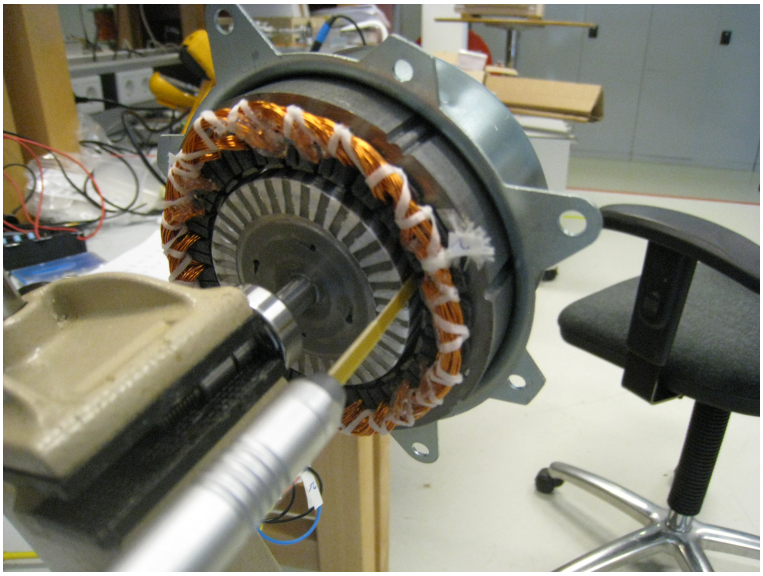

Figure 4.10: Magnetic field measurement set up.

It can be seen from the measurement that some measurement data are not as symmetrical as the simulation and modeling results. That could because of the measuring inaccuracy. During the measuring process, it has been noticed that at some positions, the display on Gauss meter varies a lot. Besides, due to the stator is rotated by hands, it is difficult to control the rotating angle. Thus, the measurement results here can only provide a general view for the real magnetic field and it is more or less similar with the tendency from simulations in Figure 3.6 in Chapter 3. The effect of the magnetic field should be verified further with the rotor to see the motor performance.

4.5. Conclusions

This Chapter proposes the winding scheme based on the design results from Chapter 3. Several winding methods are listed and compared. There are always trade off between different winding schemes. The choice should be made based on the motor characteristic, requirements and the solving problems. The chosen winding method in this research is aiming at solving the research problem while easier to realize by hands. It successfully verifies the effectiveness of the design method in Chapter 3. Besides, the magnetic field generated by the windings is measured with Gauss meter to give a general insight about the real situations. Up to this Chapter, the winding and stator are ready to be tested with the rotor.

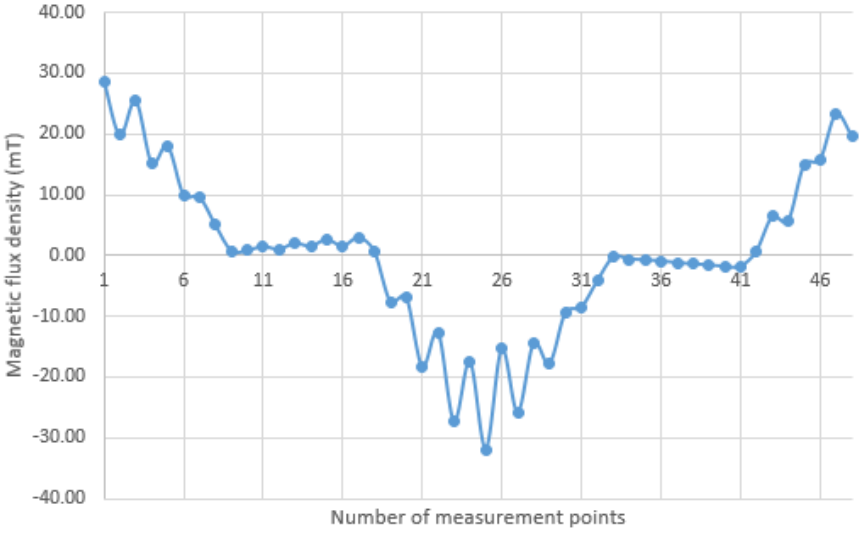

(a) Magnetic field measurement results for winding one.

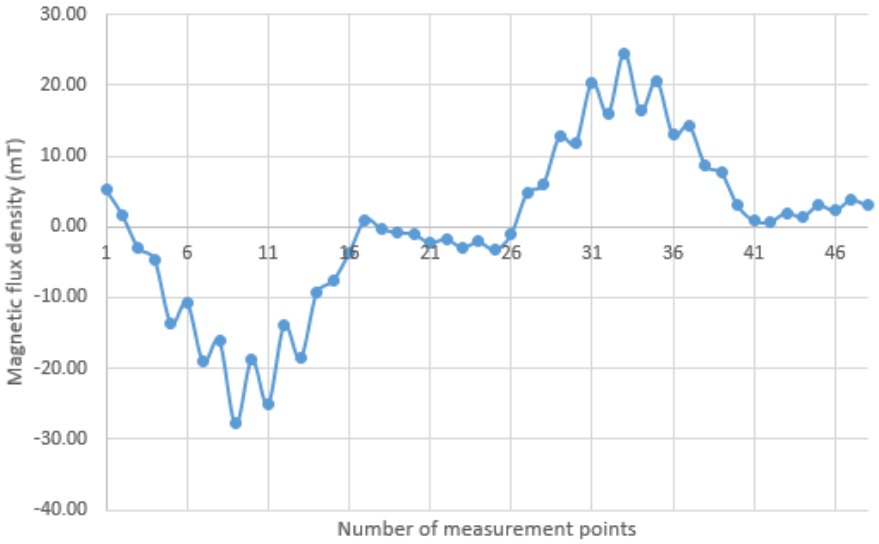

(b) Magnetic field measurement results for winding two.

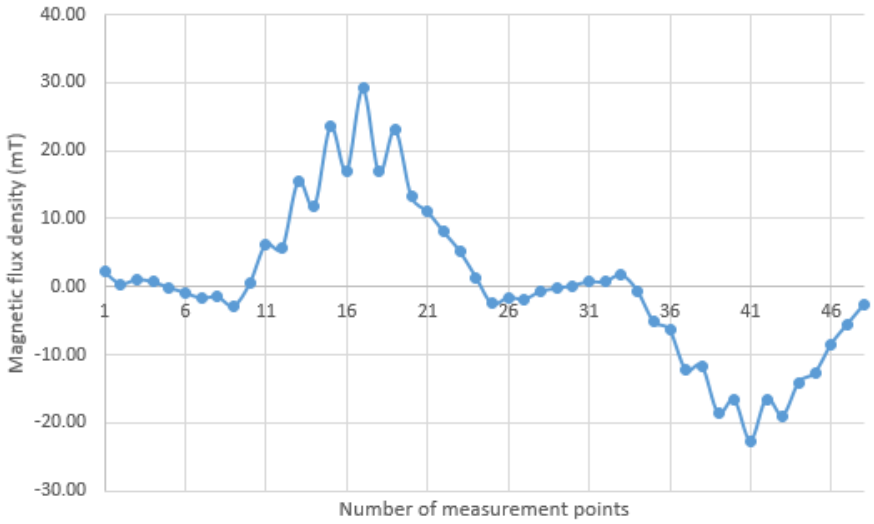

(c) Magnetic field measurement results for winding three.

Figure 4.11: Magnetic field measurement results for windings with Gauss meter.

5

Rotor design and prototype tests

The special designed rotor for six slots stator is shown in Figure 1.1b. To test the feasibility of the structure, the design of the new rotor for 24 slots stator is based on Figure 1.1b while only some small changes are made and the size are redesigned. This Chapter gives a intuitive sketch of the new rotor and reasons the size values. Based on the design, the prototype is made by the workshop from Philips. In the end, the rotor prototype is combined with the stator shown in Figure 4.9 and several tests are conducted on the prototype.

5.1. Rotor sketch and description

Figure 5.1 is the sketch of the rotor for 24 slots stator. It contains iron laminations, copper layer and two end copper rings. The structure is more or less similar with the rotor for 6 slots stator. The only difference is that the end ring is designed to be part of the copper layer rather than a separate ring. The purpose is to reduce the power dissipation in this return path. At the same time, to make it convenient to mount the rotor into the stator, one copper ring is designed outside the copper layer while the other one is designed inside of the copper layer.

The purpose of the end ring is to form a return path for the eddy current. But the resistance for the end ring should be much smaller than the copper layer to reduce the dissipation on this return path. The height of the stator teeth is 23.2mm. Then, the total height of the copper layer is $l_{layer} = 23.2 + 15 + 5 = 43.2mm$. Take the cross section area under one stator tooth as an example. The pole angle is 10.9°. The cross section area can be calculated with formula 5.1.

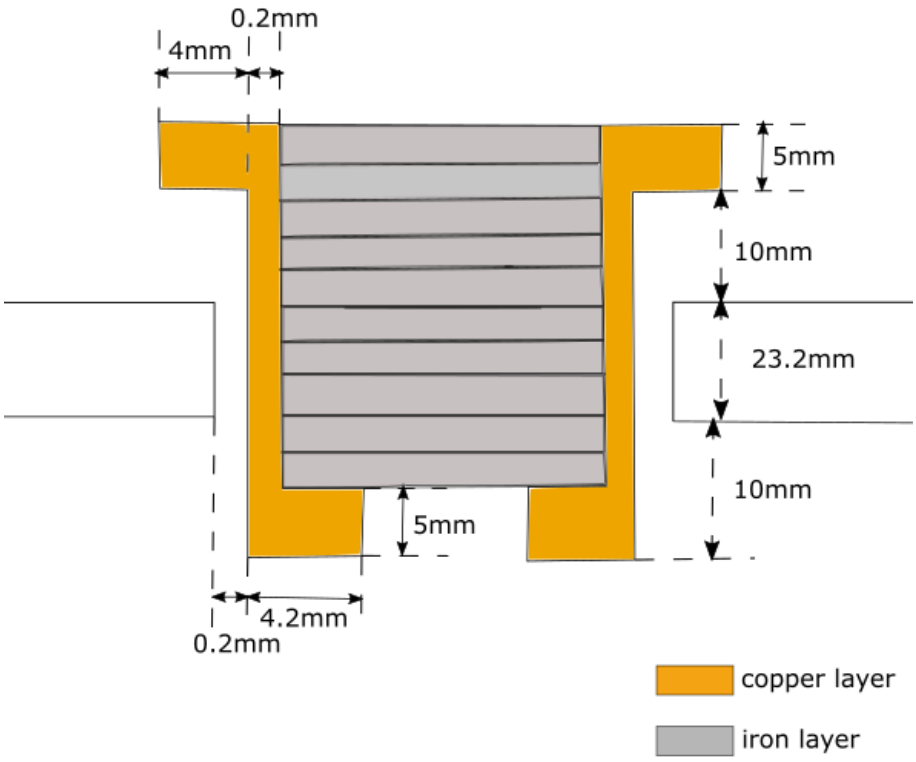

Figure 5.1: Sketch for the new rotor.

$$\begin{aligned} S &= \frac{\theta}{360^\circ}(\pi R_1^2 - \pi R_2^2) \\ &= \frac{10^\circ}{360^\circ} * (\pi * 29.8^2 - \pi * 29.6^2), \end{aligned} \tag{5.1}$$

where θ is the pole angle; R_1 is the outer radius of the copper layer which is 29.8mm and R_2 is the inner radius of the copper layer which is 29.6mm. Then the cross section area can be calculated as $1.13mm^2$. The resistance of the copper layer under one stator tooth can be calculated with formula 5.2. l is the height of the copper layer which is 43.2 mm; S is the cross section area which has been calculated as $1.13mm^2$, and ρ is the resistivity of the copper, $1.68 \times 10^{-8}\Omega \cdot m$. The resistance can be calculated as $64.2265 \times 10^{-5}\Omega$.

$$\begin{aligned} R &= \rho\frac{l}{S} \\ &= 1.68 \times 10^{-8}\frac{43.2 \times 10^{-3}}{1.13 \times 10^{-6}} \\ &= 64.2265 \times 10^{-5}\Omega \end{aligned} \tag{5.2}$$

The thickness of the copper ring in Figure 5.1 is 4mm and the height is 5mm. Based on the same calculation principle, the resistance under one stator tooth of the copper ring can be calculated as $0.5082 \times 10^{-5}\Omega$. The resistance of the

copper ring is much smaller than the copper layer. Thus, the size of the copper ring and copper layer in Figure 5.1 is reasonable.

The iron layer can be made as an iron ring, i.e., the inside space of the iron ring can be left as hollow. In that case, the iron ring should be thick enough to prevent the magnetic flux saturation. Based on the formula $\Phi = B * A$, the maximum flux B_{max} in this circumstance should be less than the saturation magnetic field value times the minimum surface area A_{min}, which can be expressed as Equation 5.3. Here the saturation magnetic field value is chosen as 1.8 T, which is large enough for the iron material under this research and $d_{ironmin}$ indicates the minimum thickness of the iron ring.

$$\begin{aligned} &\Phi_{max} < B_{max} \times A_{min} \\ &\Phi_{max} < 1.8T \times (43.2 - 5)mm \times d_{ironmin}. \end{aligned} \tag{5.3}$$

It can be assumed that the thickness of the iron ring is 10 mm. Based on the simulation results, the maximum magnetic field density value is 0.241T for one phase winding under one stator teeth. Considering there are three phase windings, to give enough space of the B field values, the maximum value is chosen as 0.241*3T. The surface area under one pole for the iron ring is

$$S = \frac{10^\circ}{360^\circ} * 2 * \pi * 29.6 * (43.2 - 5) \quad = 215.1092mm^2. \tag{5.4}$$

The Equation 5.3 can be expressed as

$$0.241T * 3 * 215.1092mm^2 < 1.8T * (43.2 - 5)mm * d_{ironmin}.$$

$$d_{ironmin} > 2mm.$$

Thus, if the iron layer is designed as iron ring, then the thickness can be chosen as 10mm. Above provides the calculation if the the iron layer needed to be designed as iron ring. But for the convenience of the testing and coupling, the rotor prototype in this research is filled with iron, as shown in Figure 5.2. The outer yellow material is copper and the inside golden material is non-magnetic material which is used to fix the iron layers inside and put everything together. The bearing and shaft are used to fix the rotor with the housing and couple with loads.

5.2. Prototype test

Considering the flux linkage, the rotor is designed to be at the axial height of the stator. Also, to make sure the end copper ring does not conflict with the winding, the end ring on the top is higher than the winding. Due to the size of the new rotor is larger than the squirrel cage rotor used before and the materials are also different, the new rotor is heavier than the squirrel cage rotor, which also means this rotor has more inertia. With the new rotor and

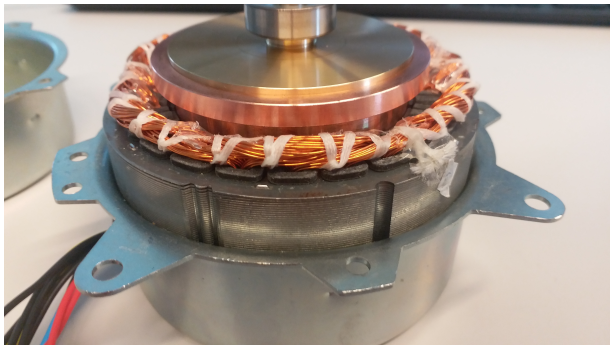

Figure 5.2: New designed rotor prototype with stator.

the 24 slots stator, several tests are conducted in this section to test motor performance.

A basic test is conducted first to see the motor rotational speed under no load. The test set up is shown in Figure 5.3. Rpm meter is used to display the rotational speed. An electronics device is used to generate the three phase voltage while the electrical driving frequency can be changed. At the same time, a thermal meter is used to monitor the winding temperature in case of the damage of the isolation due to the high temperature. The test data are shown in Table 5.1.

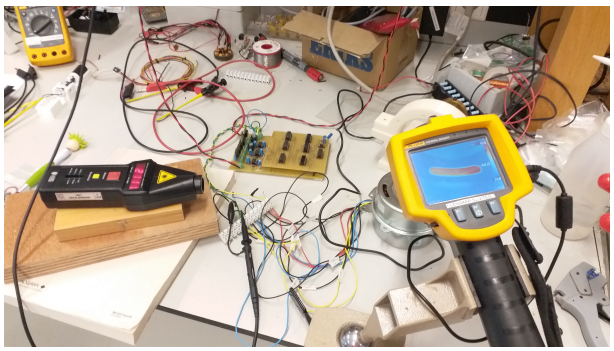

Figure 5.3: Test set up while the motor is not coupled with DC motor.

Table 5.1: No load test for 24 slots asynchronous motor with different electrical frequency

Electrical frequency (Hz)	45	55	65	75	85	95
Rotational speed (rpm)	2314	2783	3258	3728	4260	4728

It can be seen from Table 5.1 that the motor can operate around 83% of the synchronous speed with the input rail voltage of 14V from power supply. For the higher frequency, more voltage and current are needed to get closer to the synchronous speed while the winding temperature needs to be taken care of.

Then the synchronous motor is coupled with a DC motor as in Figure 5.4. The motor constant is calculated by using the asynchronous motor to drive

the DC motor. Record the rotational speed and the voltage generated by the DC motor. Then based on the ratio between the generated voltage and the rotational speed, motor constant k_{em} for the coupled DC motor can be obtained as $0.014226N \cdot m/A$. The test data are shown in Table 5.2.

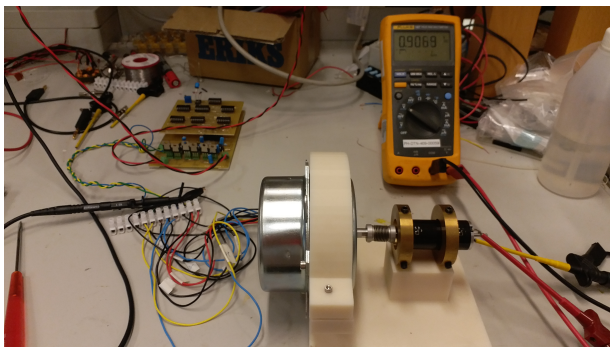

Figure 5.4: Test set up while the motor is coupled with DC motor.

Table 5.2: Rotational speed and generated voltage by DC motor under different electrical frequency.

Electrical frequency (Hz)	55	65	75	85
Rotational speed (rpm)	2759	3202	3686	4178
Generated voltage (V)	4.11	4.76	5.49	6.23

To get the friction parameters while the asynchronous motor coupled with DC motor, the set up in Figure 5.4 is still used while DC motor is used to drive the asynchronous motor. The input DC voltage, current and rotational speed is listed in Table 5.3.

Table 5.3: Input DC voltage and current and corresponding rotational speed

Input DC voltage (V)	1	2	3	4	5	6	7
Input DC current (A)	0.16	0.23	0.3	0.31	0.35	0.4	0.43
Rotational speed (rpm)	501	1154	1730	2313	2980	3655	4290

Because the DC motor constant k_{em} has been obtained as $0.014226N \cdot m/A$, the coulomb friction torque T_c and viscous friction coefficient R_v can be obtained based on the rotational speed and input DC current from Table 5.3. After the calculation, T_c is $2.131 * 10^{-3}N \cdot m$ and R_v is $1.108 * 10^5 rad/s \cdot N \cdot m$. With the above friction parameters and the motor constant. The load curve is tested according to the circuit as shown in Figure 5.5. A DC power supply provides the voltage and the current to the inverter. Then the inverter generates the three phase voltage. The coupled DC motor can be taken as a load and it can also be used to provide more torque to help or against the asynchronous motor. The test data are shown in Table 5.4. Based on the motor constant K_{em}, friction parameters T_c and R_v, the pure torque generated by the asynchronous motor can be calculated with the Equation 5.5. Then the testing data is plotted in Figure 5.6 in dots. The red dots are the results under different loads

with various resistance. The green dots are the results of using the DC motor to help the asynchronous motor accelerate to higher speed. The yellow dots are the results of using the DC motor to brake the asynchronous motor to reach lower speed or rotate in the other direction.

$$T_{load} = K_{em} * I_{load} + T_c + \frac{\omega}{R_v}. \tag{5.5}$$

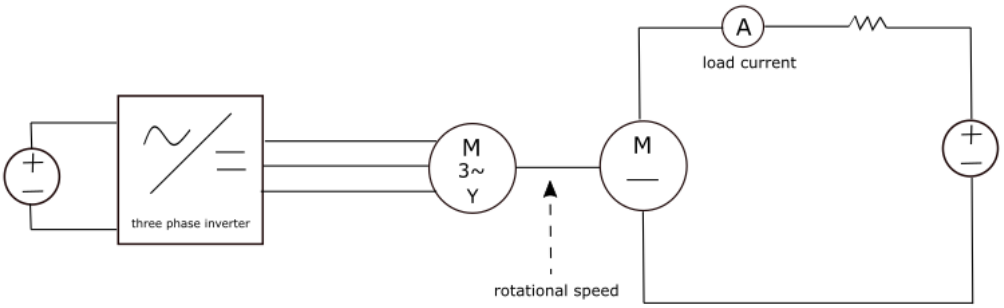

Figure 5.5: Test circuit for asynchronous motor load curve.

Table 5.4: Load curve test data

Load current (A)	-1.99	-1.33	-1.01	-0.28	0	0.015	0.029	0.058
Rotational speed (rpm)	3540	3420	3360	3176	3023	2974	2972	2965
Load current (A)	0.126	0.277	0.490	0.73	0.83	0.87	0.92	0.85
Rotational speed (rpm)	2939	2875	2742	2518	2356	2107	1587	1245
Load current (A)	0.9	0.84	0.87	0.97	1.01	1.04		
Rotational speed (rpm)	865	850	261	0	-309	-580		

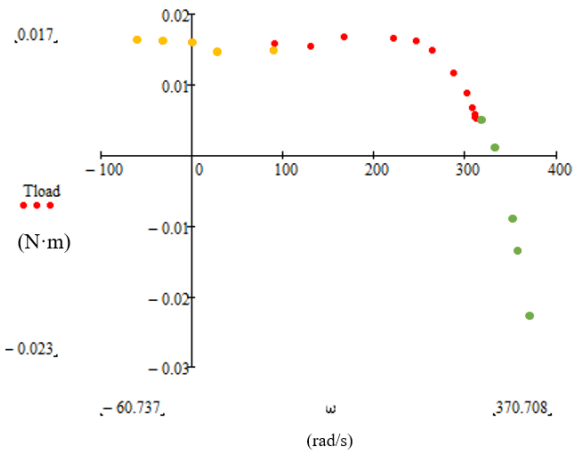

Figure 5.6: Asynchronous motor load curve.

It can be noticed form the load curve that the starting torque is comparably high, which helps the motor speed up quite fast. The motor can reach around 3023rpm by itself under the rail voltage of 14V and the driving frequency of 60Hz. By using the DC motor to provide more torque to the asynchronous motor, it can reach around the synchronous speed.

5.3. Conclusions

The rotor for the 24 slots stator is described in this Chapter. The new rotor has some differences with the rotor for the six slots stator. Such as the position of the two end rings. One ring is outside of the copper layer and one is inside, which makes the end ring as part of the copper layer to reduce the eddy current loss. With the wound stator shown in Chapter 4, the prototype is tested and the results are shown in tables and plots. It can be seen that the motor can operate around 83% of the synchronous speed under 14V rail voltage and 3.10A from DC power supply. The prototype performance is much better than the six slots asynchronous motor presented in Chapter 2. Thus, the rotor structure is functional and the winding scheme indeed helps with the motor performance. For further improvement, better winding scheme can be applied to use the slots space more efficiently. Then it is possible to put more voltage and current, which may help widen the motor operating frequency. Up to this Chapter, the prototype has been tested and the performance is satisfactory.

6

Development of the analytical model

In Section 2.2, the analytical model is built to have a general understanding about the motor performance without involving simulation data. However, that model is too ideal to reflect the influence of the higher harmonics. Thus simulation result from ANSYS is imported to the analytical model to support the analysis. But the description from simulation does not cope well with the mathematical expressions. For example, the analytical model describes a certain stator teeth shape with the parameters such as the length and the angle of the stator shoes. While in ANSYS simulation, those information are already been considered. This Chapter shows a better developed model with another method, and the modeling results can be compared with the prototype measurements. The modeling derivations can be found in [25] and this Chapter gives a general description about the modeling process and method.

6.1. Power balance

Power balance is used to check the correctness of the modeling. The input power minus the power dissipation (power losses) should equal to the output power. A circuit diagram in Figure 6.1 is used to give a general explanation.

P_{in} represents the input power; P_{rw} indicates the power loss due to the stator winding resistance R_w, and L_w is the inductance of the coil winding. P_{innet} is the net input power after the input power minus the winding power loss, i.e., $P_{innet} = P_{in} - P_{rw}$. P_r is the power dissipation on the rotor. The R_{sri} and the L_{sri} are the response resistance and inductance for the i^{th} harmonic. The net input power minus the power dissipation on the rotor would be the output net power, which is P_{outnet}. The output power P_{out} is the results by using the output net power minus the power loss because of the friction, P_f. T_c and R_v are the coulomb friction torque and the viscous friction resistance. Power balance can be a useful tool to check the correctness of the model and it is also necessary for the efficiency calculation. The specific formulas for the

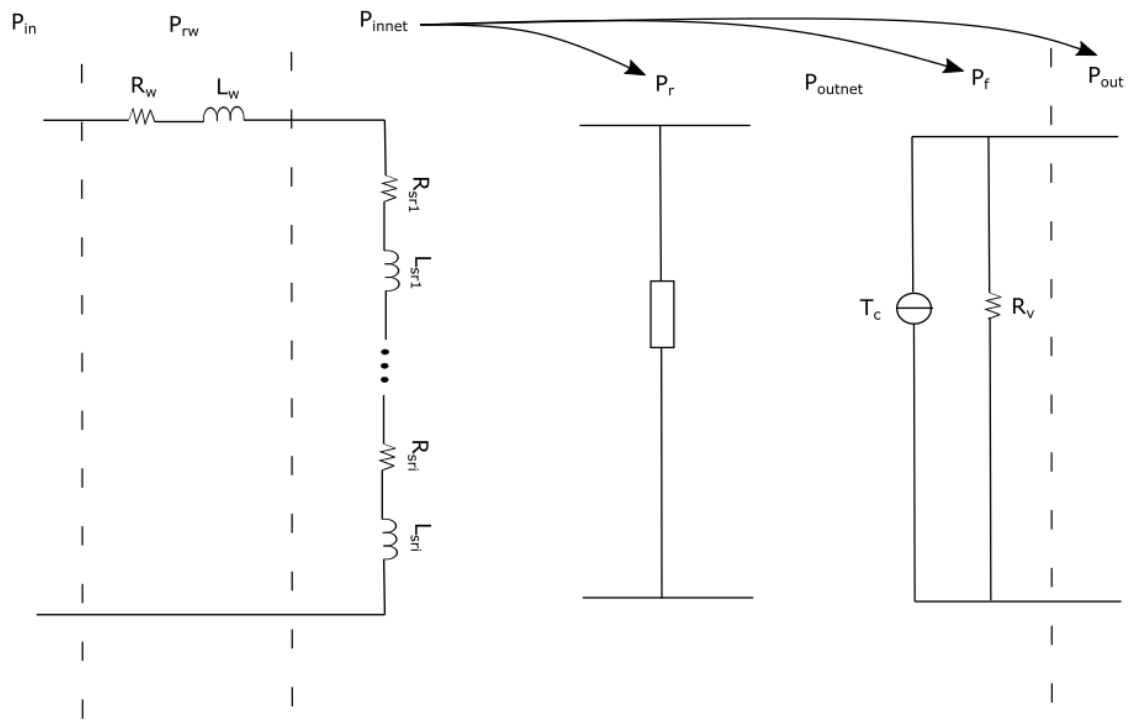

Figure 6.1: Power balance illustration.

power and parameters are described in the following sections.

6.2. Modeling description

The starting point of the modeling is the simulation data. Because the simulation already takes the winding distribution and the stator structure into consideration, the stator for modeling can be simplified as shown in Figure 6.2.

In Figure 6.2, x is position of the coil turn on the stator along the circumference. $J(x)$ is the current density and h is the thickness of the stator. The corresponding current I can be expressed as Equation 6.1. λ is the perimeter of the stator.

$$I = \int_0^{\lambda/2} J(x) * h dx. \tag{6.1}$$

As what is presented in Equation 3.2 in Chapter 3, the magnetic field generated by the current in Equation 6.1 can be expressed as

$$B(x) = \sum_{i=0}^{i=nh} a_i cos(ikx), \tag{6.2}$$

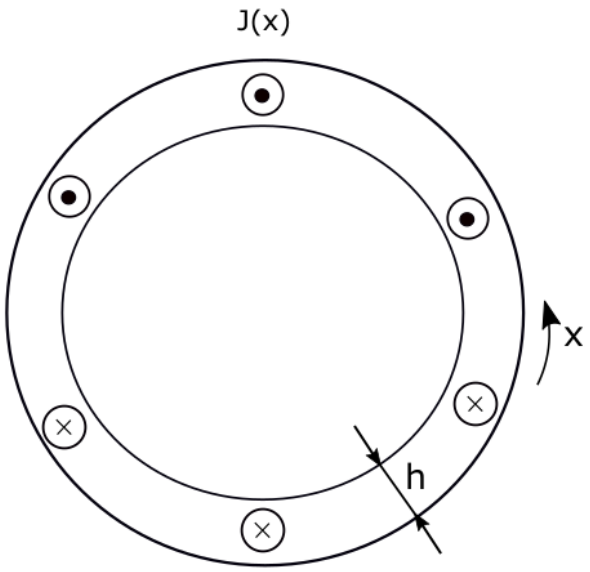

Figure 6.2: Stator illustration for modeling.

where k is $2\pi/\lambda$. Equation 6.2 describes the magnetic field with 1A DC current and certain winding turns. In a more general situation, a factor I_{DC}/I_{ref} is needed. I_{DC} is the given DC current in the simulation and I_{ref} is the current which goes through the one coil turn in the FEM model. To simplify the modeling derivation and verify the method, the derivation is first based on the assumption that only one coil turn is on the stator. After the development, the model can be expanded into the desired number of turns.

With the factor I_{DC}/I_{ref}, the magnetic field in Equation 6.2 can be expressed as

$$B(x) = \frac{I_{DC}}{I_{ref}} \sum_{i=0}^{i=nh} a_i cos(ikx), \tag{6.3}$$

where I_{ref} can be derived as Equation 6.4.

$$I_{ref} = 2\frac{\delta}{\mu} \sum_{i=i(odd)}^{i=nh} a_i. \tag{6.4}$$

δ represents the total thickness of the air gap and copper layer. For the convenience of derivation, the copper layer and the air gap are taken as an entirety, thus μ is the averaged permeability of the copper and the air. $i(odd)$ indicates that only odd harmonics are considered because of the symmetrical structure. By doing the integral of the magnetic field density in Equation 6.3 on the corresponding surface area, which is

$$\phi = \int_{-x}^{x} w * B(x) * l dx, \tag{6.5}$$

where l is the height of the rotor and w is a weight factor. The corresponding flux can be obtained as ϕ in Equation 6.6.

$$\phi = \frac{I * \pi * l * \sum_{i=1}^{i=nh} a_i^2}{2 * k * I_{ref} * \sum_{i=i(odd)}^{i=nh} a_i}. \tag{6.6}$$

The flux can also be expressed as $\phi = L_i * I$, where L is the self-inductance. Self-inductance for every harmonic can be derived as Equation 6.7.

$$L_i = \frac{\pi * l * \mu * a_i^2}{4 * k * \delta * (\sum_{i=i(odd)}^{i=nh} a_i)^2}, \tag{6.7}$$

The three phase current can be represented as Equation 6.8, where $\omega_s = 2 * \pi * f_s$ and f_s is the driving frequency.

$$\begin{aligned} I_1 &= \hat{I} * sin(\omega_s t), \\ I_2 &= \hat{I} * sin(\omega_s t - \frac{2 * \pi}{3}), \\ I_3 &= \hat{I} * sin(\omega_s t + \frac{2 * \pi}{3}). \end{aligned} \tag{6.8}$$

Based on Equation 6.3 and the expression of the three phase AC current in Equation 6.8, the traveling magnetic field B_{si} generated by the stator winding can be obtained as Equation 6.9.

$$B_{si}(x) = \frac{3 * \hat{I} * a_i * sin(\omega_s t - \zeta(i) * i * k * x)}{2 * I_{ref}}, \tag{6.9}$$

where $\zeta(i)$ is defined as Equation 6.10. The function $\zeta(i)$ is used to express that the harmonics which are the multiples of three have no influence on the results because the system is a three phase system, and it also expresses the directions of the traveling wave.

$$\zeta(i) = \begin{cases} 1, & \text{if } i \ div \ 3 = 1 \\ -1, & \text{if } i \ div \ 3 = 2 \\ 0. & \text{otherwise} \end{cases} \tag{6.10}$$

Then with a phase shift angle φ between the magnetic field generated by the stator winding and response magnetic field on the rotor, the expression for the response field on the rotor B_{ri} can be expressed as Equation 6.11.

$$B_{ri}(x) = \frac{-3 * \hat{I} * a_i * cos(\varphi_i) * sin(\omega_s t - \zeta(i) * i * k * x + \varphi_i)}{2 * I_{ref}}. \tag{6.11}$$

Following the same integral rule as Equation 6.5, the response magnetic flux ϕ_{sri} induced by B_{ri} can be got. Then equation 6.12 is used to get the response voltage U_{sri} generated by the response flux for every harmonic.

$$U_{sri} = \frac{d\phi_{sri}}{dt}. \tag{6.12}$$

At the same time, the response voltage peak value U_{sri} can also be expressed in the form of Equation 6.13.

$$\hat{U}_{sri} = R_{sri} * \hat{I} * sin(\omega_s t) + \omega_s L_{sri} * \hat{I} * cos(\omega_s t). \tag{6.13}$$

R_{sri} and L_{sri} are the response resistance value and inductance value for every harmonic; $\hat{I}$ is the peak value of the input current.

With Equation 6.12 and Equation 6.13, the response resistance and inductance can be expressed as Equation 6.14 and Equation 6.15.

$$R_{sri} = \frac{3 * \omega_s * L_i * cos(\varphi_i) * sin(\varphi_i)}{2}. \tag{6.14}$$

$$L_{sri} = \frac{-3 * \omega_s * L_i * cos^2(\varphi_i)}{2}. \tag{6.15}$$

According to Equation 6.11 and the Maxwell's equations, the eddy current density J_{ri} can be obtained as Equation 6.16.

$$J_{ri} = -\frac{1}{\mu}\frac{dB_{ri}(x)}{dx}. \tag{6.16}$$

Then with the eddy current density J_{ri}, which can be determined with the expression of the response magnetic field density B_{ri}; the height of the rotor l and the stator magnetic field B_{si}, the force on the rotor can be obtained by doing the integral on the stator perimeter as Equation 6.17.

$$F_i = \int_0^{\lambda} B_{si} * J_{ri} * l * \delta dx, \tag{6.17}$$

which can be expressed as Equation 6.18.

$$F_i = \frac{9 * \hat{I} * k^2 * i^2 * L_i * cos^2\varphi_i}{4 * \mu * \delta * v_{di}}, \tag{6.18}$$

where v_{di} is the speed of the traveling wave experienced by the rotor. Supposing that the traveling wave in Equation 6.9 has speed v_{si}, and the speed of the rotor is v_r, then v_{di} is the difference between v_{si} and v_r, i.e., $v_{di} = v_{si} - v_r$.

By doing the integral of the eddy current density as Equation 6.19, where the σ is the conductivity of the copper layer, the power dissipation on the conductive layer can be expressed as Equation 6.20.

$$P_{ri} = \int_0^{\lambda} \frac{J_{ri}^2 * l * \delta}{\sigma} dx. \tag{6.19}$$

$$P_{ri} = \frac{9 * \hat{I} * k^2 * i^2 * L_i * cos^2 \varphi_i}{4 * \mu * \sigma}. \tag{6.20}$$

Based on the response resistance in Equation 6.14, the net input power P_{innet} can be calculated as

$$P_{innet} = \frac{3 * \hat{I}^2 * R_{sri}}{2}. \tag{6.21}$$

Also, the net input power should equal to the total input power minus the power loss due to the winding resistance. The total input power P_{in} can be expressed as

$$P_{in} = \frac{3 * \hat{I} * \hat{U} * cos\phi}{2}, \tag{6.22}$$

where ϕ is the phase angle difference due to the resistance and the inductance of the coil winding and response. The winding power loss is

$$P_w = \frac{3 * \hat{I}^2 * R_w}{2}, \tag{6.23}$$

where R_w is the winding resistance value. The results of the net input power is expressed again as $P_{innetcal}$.

$$P_{innetcal} = P_{in} - P_w. \tag{6.24}$$

The output net power has also two calculation approaches. One is using the motor rotational speed v_R times the force experienced by the rotor, which can be expressed as

$$P_{outnet} = v_R * F_i. \tag{6.25}$$

The other way is using the net input power minus the power dissipation on the rotor. The net output power for this approach is indicated as $P_{outnetcal}$.

$$P_{outnetcal} = P_{innet} - P_{ri}. \tag{6.26}$$

P_{outnet} and $P_{outnetcal}$ should equal to each other.

Then for the final output power is

$$P_{out} = T_r * \omega_0, \tag{6.27}$$

where the torque T_r is the torque value after the friction torque; ω_0 is the rotational speed and T_f and is friction torque. Friction loss can be expressed as Equation 6.28.

$$P_f = T_f * \omega_0. \tag{6.28}$$

According to the power balance illustrated in Figure 6.1, the output power p_{out} should satisfy the equation

$$P_{outcal} = P_{in} - P_w - P_r - P_f. \tag{6.29}$$

In the meanwhile, the two approaches to calculate the input net power and output net power should give the same results. Thus P_{innet} should equal to $P_{innetcal}$ and P_{outnet} should equal to $P_{outnetcal}$. The power balance can be verified by checking if

$$\begin{aligned} P_{outcal} &= P_{out}, \\ P_{innet} &= P_{innetcal}, \\ P_{outnet} &= P_{outnetcal}. \end{aligned} \tag{6.30}$$

As mentioned above, to simplify the derivation at first, the model is built under the assumption that there is only one coil turn on the stator. In the one turn model derivations, it is assume that the current from the power supply is all the current and the self-inductance can be obtained as Equation 6.7. However, except the current from power supply, there is another current which comes from the magnetized stator iron. With the basic derivations, the model is expanded into N effective turns. At the same time, both the current from the power supply and the magnetization current are considered.

Based on the transfer ratio I_{ref}/I_{wref} defined above and the effective winding turns N on the stator, the formulas for N turns model are the same except the self-inductance. The self-inductance Ln_i for N turns situation can be defined as Equation 6.31 based on Equation 6.7. For the derivation details can be found in [25].

$$Ln_i = \frac{N * I_{ref} * \pi * l * \mu * a_i^2}{4 * I_{wref} * k * \delta * (\sum_{n=i(odd)}^{n=nh} a_i)^2}. \tag{6.31}$$

The above equations show the expressions for the i^{th} harmonic individually. By summing every i^{th} harmonic's result together from 1^{st} to nh^{th} harmonic, the results of nh harmonics together can be obtained. Considering the symmetrical geometry of the stator and the winding distribution, only odd harmonics are considered. Also due to this is a three phase system, the harmonics which are the multiples of three should not have influence on the results.

The starting point of the modeling is similar with the method raised in [26] in section 2.6 Chapter 2. A machine with a windingless cylindrical rotor is

described and the self-inductance is derived as Equation 2.50 in [26]. The self-inductance in [26] Equation 2.50 is actually the the inductance shown in Equation 6.7. Just in Equation 6.7, the effective turn is one turn and if only the fundamental harmonic is considered, two equations are exactly the same.

It is reasonable that the model starts with the ANSYS simulation data without considering stator winding structure. With the developed model, the number of the effective turns is put in the model and the modeling results are shown in the following section.

6.3. Modeling results and comparison

From Equation 6.31, the self-inductance value from the modeling can be obtained as 3.377mH for 56 harmonics. From ANSYS simulation results and based on Equation 6.32,

$$E = \frac{1}{2} * L * I^2, \tag{6.32}$$

where L is the self-inductance value; E is the stored energy in system, which can be obtained from ANSYS with APDL commands. Current I in simulation is assumed to be 1A. Thus, the self-inductance value can be obtained around 3.0861mH. To compare the value with real measurement, the measuring method used in section 2.3 is repeated here. The voltage waveform and current waveform is captured with oscilloscope. By calculating the phase angle difference between them and with Equation 2.2, the self-inductance of one winding from the measurement can be obtained around 2.973mH. The self-inductance values from modeling, simulation and measurement are close to each other. The small difference might due to the inaccuracy of the data reading, measuring or the number of harmonics used in the modeling. In general, they are in the same value level.

Based on the developed model and the tests conducted in Chapter 5, 14V rail voltage and 60HZ driving frequency are chosen as the parameters in the modeling. The number of the harmonics is 23 in the results shown below. Figure 6.3a shows the force curve experienced by the rotor from the modeling, corresponding with the Equation 6.18. To compare the torque curve with Figure 5.6 in Chapter 5, the torque shown in Figure 6.3b is calculated by using the force in Equation 6.18 times the radius of the rotor.

The input net power curves calculated in two ways corresponding with the Equation 6.21 and Equation 6.24 are shown in Figure 6.4a. It can be seen that the input net power from both ways are the same with each other. The output net power curves calculated in two ways corresponding with the Equation 6.25 and Equation 6.26 are shown in Figure 6.4b. They are also equal with each other. The results illustrate the correctness of the power balance in Equation 6.30 and also verifies the correctness of the modeling derivations. The output power in Equation 6.27 divided by the input power in Equation

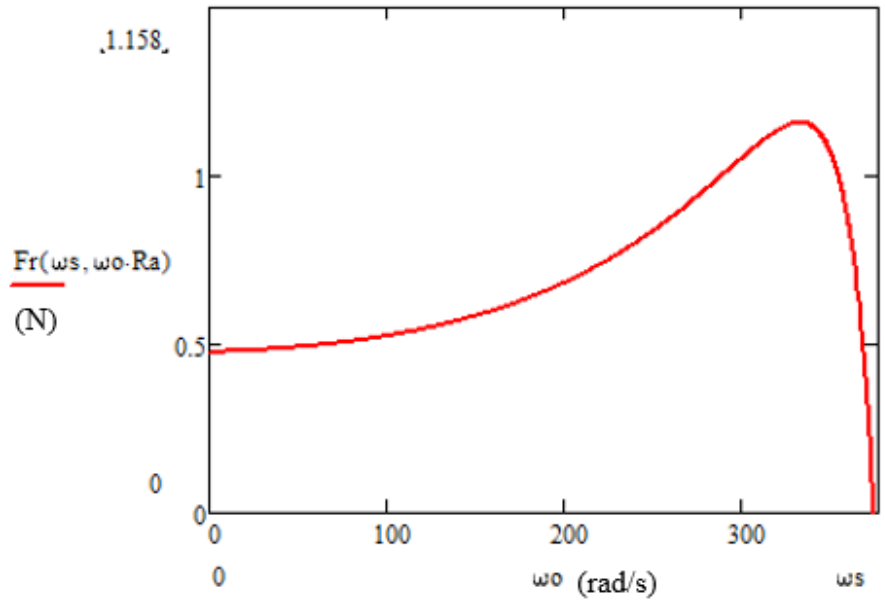

(a) Force experienced by the rotor from the analytical model.

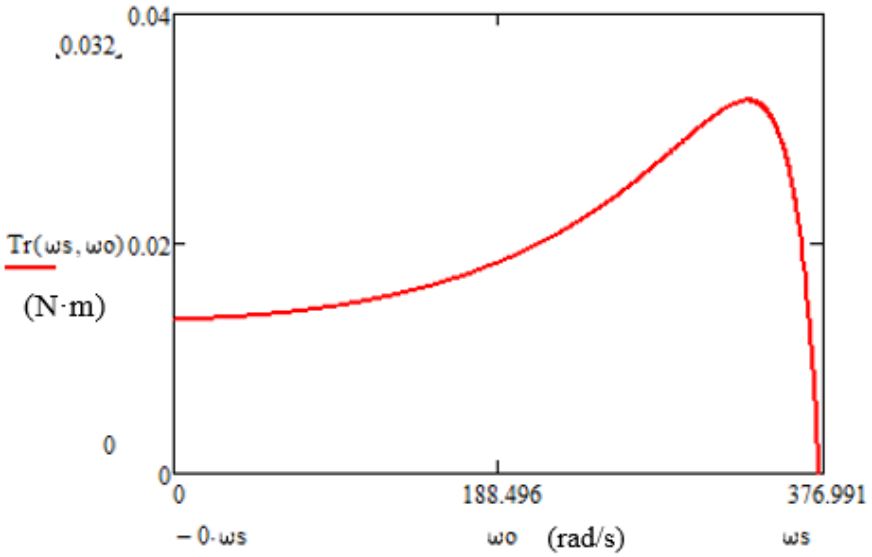

(b) Torque curve after the friction from analytical model.

Figure 6.3: Force curve and the corresponding torque curve with the friction parameters.

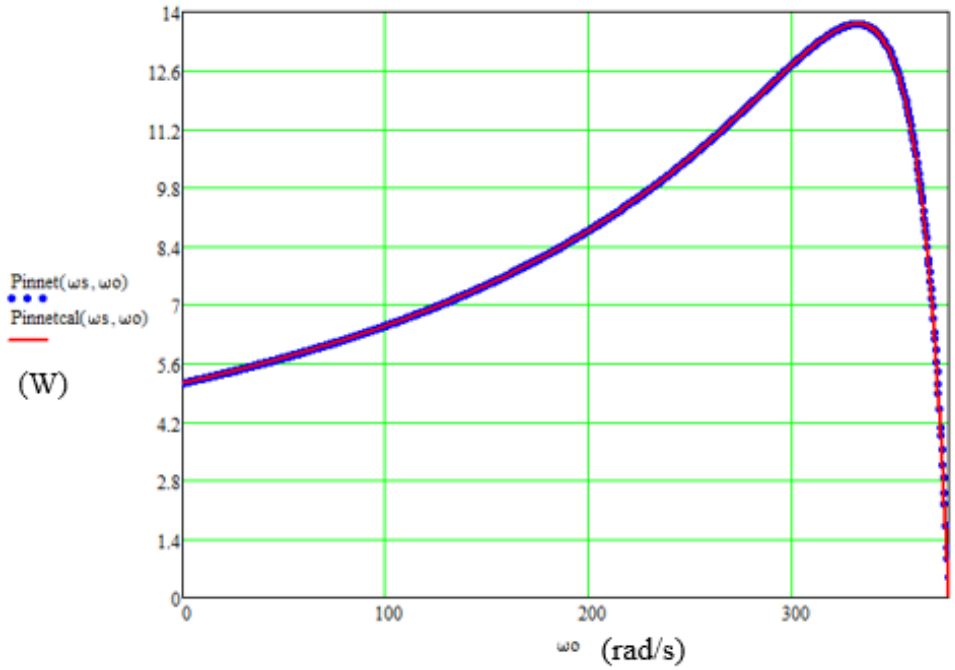

(a) Input power in analytical model.

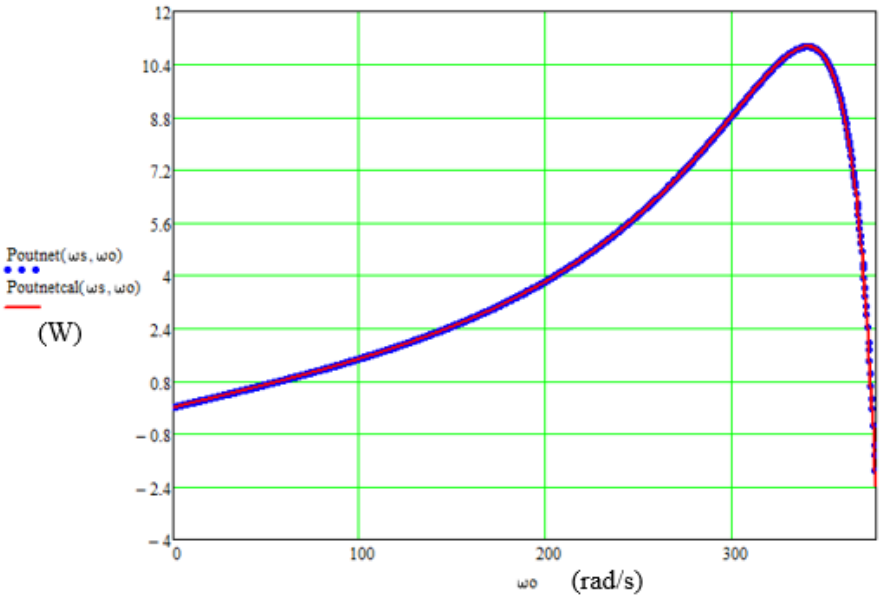

(b) Output power in analytical model.

Figure 6.4: Input power and output power from the analytical model.

6.22 leads to the efficiency curve shown in Figure 6.5.

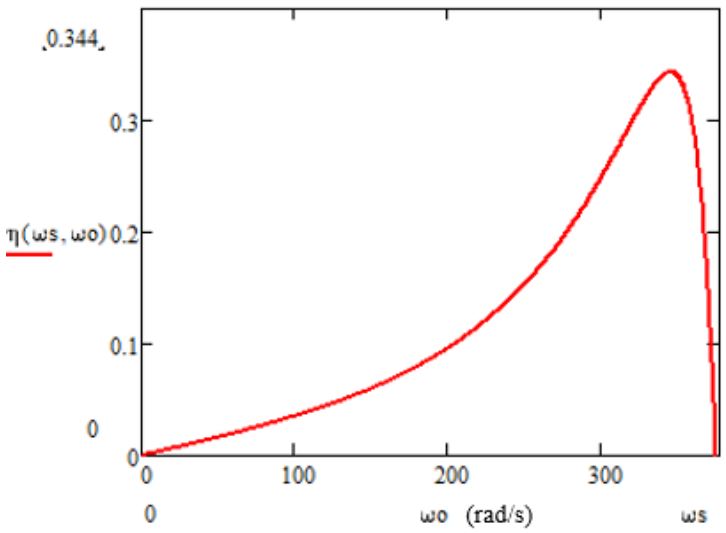

Figure 6.5: Motor efficiency based on the input power and output power.

The parameters in the modeling are set based on the prototype tests in Chapter 5. The shape of the torque speed characteristic curve in Figure 6.3b is similar with what obtained from the measurement in Figure 5.6. The torque values from the modeling are in the same magnitude with the measurement. There are some small differences, for example, the peak torque from the modeling is higher than the measurement, and the speed when the load curve across the zero is around 3000 RPM in the measurement while it is higher in the modeling. The reason which leads to the difference might be that there are some external factors in the measurement are not considered in the modeling. For example, the resistance of the connection wires, the internal resistance of the power supply and etc. But in general, the small differences are acceptable and the modeling results are close the to the situation in the real test, which gives the strong support to predict the motor behaviour under difference conditions.

6.4. Conclusions

Based on the analytical model studied in Chapter 2, the model is developed further in this Chapter. Different from the previous model, this model uses the ANSYS simulation data as the staring point and complete the modeling with rigorous derivations. The modeling results are close to the prototype test results from Chapter 5 and the correctness of the model is also verified by the power balance checking. The performance of the asynchronous motor is understood further and the model will be a useful tool for further research and studies. In the end, it is deserved to be noted that all the mathematical derivations details can be found in [25].

7

Conclusions and future work

This research starts with a six-slot asynchronous motor with certain stator winding distribution and a special rotor structure. The analytical model and the simulation with FEM are used as tools to understand the motor behavior. Subsequently, it is verified that the space harmonics have certain influence on the motor performance. Based on the previous studies and literature reviews, changing the winding configurations is a good approach to suppress the space harmonics and then a method to design the winding distribution is proposed. The motor size is changed from six slots into twenty four slots. This design is realized into prototype after some discussion on the common seen winding distribution scheme and then a new rotor for twenty four slots stator is made by the workshop.

The motor prototype can operate around 83% of the synchronous speed and the torque speed characteristic curve also indicates a well-performing motor. In the meanwhile, a better analytical model is developed. Compared with the analytical model used in the beginning, this developed model combines the simulation data and the analytical derivations in a more rigorous way. The modeling results can also correspond with the prototype test results. In general, this model can provide strong support to reflect the motor behaviors under different conditions.

Through this research, the motor performance is understood and a more complete analytical model is developed, which can be used in further research and studies. There are some directions for further work. For example, the winding distribution scheme used in this research is done by hands while it might not be suitable for the automatic industry process. A more proper winding distribution scheme can be found with the same effect. Also, if the slots space of the stator can be used more efficiently, more turns or thicker copper wires can be used. That would also help in improving the motor performance as well. All in all, the motor performance has been understood and the results can support for future studies.

Bibliography

[1] B. J. Wojtas, “The age of the squirrel cage [motors],” IEE Review, pp. 435–438, 1991.

[2] V. F. de Jesús and A. M. Omar, “Characterizing the Squirrel Cage Induction Motor,” in 2013 International Conference on Mechatronics, Electronics and Automotive Engineering, 2013, pp. 134–139.

[3] C. Zhang and N. Wang, “Research on asynchronous motor control of electric vehicle,” in 2017 International Conference on Mechanical, System and Control Engineering (ICMSC), 2017, pp. 165–169.

[4] Byung-Taek Kim, Byun-Il Kwon, and Seung-Chan Park, “Reduction of electromagnetic force harmonics in asynchronous traction motor by adapting the rotor slot number,” IEEE Transactions on Magnetics, vol. 35, no. 5, pp. 3742–3744, Sep. 1999.

[5] V. Fireteanu and P. Taras, “Finite element models of the transient heating of squirrel-cage rotor during induction motors startup,” in Automation and Motion International Symposium on Power Electronics Power Electronics, Electrical Drives, 2012, pp. 490–495.

[6] L. Varshney, C. Gupta, and D. Debnath, “Performance improvement of Squirrel cage rotor by design aspects,” in 2016 International Conference on Recent Advances and Innovations in Engineering (ICRAIE), 2016, pp. 1–4.

[7] 15 P. C Sen, “Principles of Electric Machines and Power Electronics,” John Wiley Sons, Inc., 1997.

[8] M. van der Geest, H. Polinder, and J. A. Ferreira, “Computationally efficient 3D FEM rotor eddy-current loss calculation for permanent magnet synchronous machines,” in 2015 IEEE International Electric Machines Drives Conference (IEMDC), 2015, pp. 1165–1169.

[9] Y. Kawase, T. Yamaguchi, M. Otsubo, Y. Iwai, N. Toida, and K. Sato, “Operating characteristics analysis of cage-rotor induction motor and matrix-rotor induction motor using 3-D finite element method,” in 2014 International Conference on Electrical Machines (ICEM), 2014, pp. 598–601.

[10] K. Yamazaki and M. Matsumoto, “3-D Finite Element Meshing for Skewed Rotor Induction Motors,” IEEE Transactions on Magnetics, vol. 51, no. 3, pp. 1–4, Mar. 2015.

[11] P. Luo, “Modelling and Measurement of Asynchronous Motor with Special Rotor Structure | TU Delft Repositories,” 2017. [Online]. Available: http://resolver.tudelft.nl/uuid:401d2205-98e6-46cc-bd45-59691cdc13cb.

[12] S. N and C. Lakshminarayana, “An Insight to Harmonic Suppression Techniques with Power Filters in Power Electronics,” International Journal of Computer Applications, vol. 111, pp. 26–34, 2015.

[13] R. Buinac and V. Tomljenović, “Determination of the torque-speed characteristic of induction motor in electric machinery education,” in 2013 36th International Convention on Information and Communication Technology, Electronics and Microelectronics (MIPRO), 2013, pp. 765–769.

[14] P.J. Bax, “Modelling approaches for multi-domain systems,” internal report from Philips TEG.

[15] X. Wang, D. Liu, D. Lahaye, H. Polinder, and J. A. Ferreira, “Finite element analysis and experimental validation of eddy current losses in permanent magnet machines with fractional-slot concentrated windings,” in 2016 19th International Conference on Electrical Machines and Systems (ICEMS), 2016, pp. 1–6.

[16] X. Wang, T. D. Strous, D. Lahaye, H. Polinder, and J. A. Ferreira, “Harmonics study of nested-loop rotors in brushless doubly-fed induction machines,” in 2016 XXII International Conference on Electrical Machines (ICEM), 2016, pp. 371–377.

[17] T. D. Strous, X. Wang, H. Polinder, and J. A. Ferreira, “Evaluating Harmonic Distortions in Brushless Doubly Fed Induction Machines,” IEEE Transactions on Magnetics, vol. 53, no. 1, pp. 1–10, Jan. 2017.

[18] Alan V. Oppenheim, Alan S. Willsky and S.Hamid Nawab, “Signals and systems,” Prentice Hall, 1997.

[19] M. Valtonen, A. Parviainen, and J. Pyrhonen, “The Effects of the Number of Rotor Slots on the Performance Characteristics of Axial-Flux Aluminium-Cage Solid-Rotor Core Induction Motor,” in 2007 IEEE International Electric Machines Drives Conference, 2007, vol. 1, pp. 668–672.

[20] L. Varshney, C. Gupta, and D. Debnath, “Performance improvement of Squirrel cage rotor by design aspects,” 2016, pp. 1–4.

[21] M. Y Mohamed, S. A Abdel Maksoud, M. Fawzi, and A. E Kalas, “Effect of Poles, Slots, Phases Number and Stack Length Changes on the Optimal Design of Induction Motor,” 2017.

[22] A. E. Fitzgerald, C. Kingsley, and S. D. Umans, “Electric Machinery,” McGraw-Hill, 2003.

[23] J. Srinivasan, K. Selvaraj, J. Chitrarasu, and R. Resmi, “Design and analysis of squirrel cage induction motor in short pitch and full pitch winding configurations using FEA,” in 2016 International Conference on Emerging Technological Trends (ICETT), 2016, pp. 1–10.

[24] X. Wang, D. Liu, D. Lahaye, H. Polinder, and J. A. Ferreira, “Finite element analysis and experimental validation of eddy current losses in permanent magnet machines with fractional-slot concentrated windings,” in 2016 19th International Conference on Electrical Machines and Systems (ICEMS), 2016, pp. 1–6.

[25] P.J. Bax, “Analytical harmonic model for an asynchronous motor,” internal report from Philips TEG.

[26] M.J. Hoeijmakers, “Modelling of AC machines,” Delft University of Technology, 2004.